AGU PUBLICATIONS

JGR

Journal of Geophysical Research: Oceans

RESEARCH ARTICLE

10.1002/2017JC013476

Eddy-Kuroshio Interactions: Local and Remote Effects

Sen Jan[1], Vigan Mensah[1,2], Magdalena Andres[3], Ming-Huei Chang[1], and Yiing Jang Yang[1]

[1]Institute of Oceanography, National Taiwan University, Taipei, Taiwan, [2]Now at Institute of Low Temperature Science, Hokkaido University, Sapporo, Japan, [3]Woods Hole Oceanographic Institution, Woods Hole, MA, USA

Key Points:
- Observations of eddy-Kuroshio interactions are interpreted through numerical simulations with varying eddy strength and impinging latitude
- Locally, eddy arrivals change sea level and isopycnal depths leading to seesaw-like patterns across the Kuroshio
- Modeled remote effects manifest at the Luzon Strait and East China Sea shelf and depend on the eddies' impingement latitude and polarity

Correspondence to:
S. Jan
senjan@ntu.edu.tw

Citation:
Jan, S., Mensah, V., Andres, M., Chang, M.-H., & Yang, Y. J. (2017). Eddy-Kuroshio interactions: Local and remote effects. *Journal of Geophysical Research: Oceans*, *122*, 9744–9764. https://doi.org/10.1002/2017JC013476

Received 20 SEP 2017
Accepted 17 NOV 2017
Accepted article online 30 NOV 2017
Published online 11 DEC 2017

Abstract Quasi-geostrophic mesoscale eddies regularly impinge on the Kuroshio in the western North Pacific, but the processes underlying the evolution of these eddy-Kuroshio interactions have not yet been thoroughly investigated in the literature. Here this interaction is examined with results from a semi-idealized three-dimensional numerical model and observations from four pressure-sensor equipped inverted echo sounders (PIESs) in a zonal section east of Taiwan and satellite altimeters. Both the observations and numerical simulations suggest that, during the interaction of a cyclonic eddy with the Kuroshio, the circular eddy is deformed into an elliptic shape with the major axis in the northwest-southeast direction, before being dissipated; the poleward velocity and associated Kuroshio transport decrease and the sea level and pycnocline slopes across the Kuroshio weaken. In contrast, for an anticyclonic eddy during the eddy-Kuroshio interaction, variations in the velocity, sea level, and isopycnal depth are reversed; the circular eddy is also deformed to an ellipse but with the major axis parallel to the Kuroshio. The model results also demonstrate that the velocity field is modified first and consequently the SSH and isopycnal depth evolve during the interaction. Furthermore, due to the combined effect of impingement latitude and realistic topography, some eddy-Kuroshio interactions east of Taiwan are found to have remote effects, both in the Luzon Strait and on the East China Sea shelf northeast of Taiwan.

Plain Language Summary Mesoscale eddies are everywhere in the ocean. These ocean swirls of either clockwise or counterclockwise spinning with diameter of about 100-300 km and rounding current speed of about 0.5 m/s, carrying energy and certain type of water mass, move westward and eventually reach the western boundary of each ocean. The evolution of these eddies and the interaction which occurs when they encounter the western boundary current, e.g. the Kuroshio in the western North Pacific, is important in redistributing ocean energy and, in turn, shaping the large scale ocean circulation. This study focuses on the processes underlying the interaction of nonlinear mesoscale eddies with the Kuroshio, which have not yet been thoroughly investigated in the literature. Using pressure-sensor equipped echo sounder and satellite observations interpreted in the context of semi-idealized numerical simulations, this study find (1) locally, eddy arrivals modify velocity structure in the Kuroshio first, followed by changes in sea level and isopycnal depths leading to seesaw-like variations of the sea level and density slopes across the Kuroshio, and (2) modeled remote effects, i.e., Kuroshio intrusions, manifest in the Luzon Strait and on the East China Sea shelf and depend on the eddies' impingement latitude, strength, and polarity.

1. Introduction

Most mesoscale eddies in the northwestern Pacific Ocean are generated in a shear zone between the Subtropical Countercurrent (STCC) and North Equatorial Current (NEC), from 18°N to 26°N, through baroclinic and barotropic instabilities (Gill et al., 1974; Qiu, 1999; Qiu & Chen, 2010; Roemmich & Gilson, 2001). Once spun-up, these eddies, which carry energy and water mass, propagate westward at a mean translation speed of O(0.1 m s^{-1}), with a mean radius of ~130 km for cyclonic eddies (CEs) and ~120 km for anticyclonic eddies (AEs), and a mean lifespan of about 11 weeks (Cheng et al., 2014; Hwang et al., 2004; Yang et al., 2013). Some eddies are further strengthened when approaching the North Pacific western boundary (Yang et al., 2013), where they impinge on the Kuroshio (Andres et al., 2017; Cheng et al., 2017; Jan et al., 2015; Lien et al., 2015; Liu et al., 2012; Ramp et al., 2017; Tsai et al., 2015), and are ultimately dissipated in the Kuroshio through eddy-Kuroshio interactions (Tsai et al., 2015; Waseda et al., 2002) or, although this is

debated, penetrate through the Kuroshio in the Luzon Strait under certain conditions (Liu et al., 2012; Sheu et al., 2010). Understanding the generation, evolution, and fate of eddies is key to revealing how these eddies redistribute the ~1 TW (10^{12} W) energy input from surface wind stresses to the upper ocean, and to better determining the energy budget in the global ocean (Clément et al., 2016; Wunsch, 1998). The dynamic link between mesoscale eddies and small-scale turbulence is the key to determining the ocean's energy budget, yet this link is filled with many uncertainties and open questions (Clément et al., 2016).

Mesoscale eddies in the North Pacific also contribute to the synoptic to intraseasonal variability in the Kuroshio east of Taiwan, as examined using the observations at the WOCE PCM-1 line (Johns et al., 2001; Liu et al., 2004; Yang et al., 1999; Zhang et al., 2001), satellite data analysis combined with numerical model studies (Chang et al., 2015; Chang & Oey, 2012; Cheng et al., 2017; Hsin et al., 2013; Kuo et al., 2017; Lee et al., 2013; Yan et al., 2016), and recent ship-based and mooring observations both at the KTV1 line (~23.75°N) east of Taiwan (Andres et al., 2017; Jan et al., 2015; Tsai et al., 2015) and along a zonal transect off the northeast coast of Luzon (Lien et al., 2015). Despite a debate between Chang et al. (2015) and Hsin et al. (2013) about the cause of the interannual variability of Kuroshio transport, most of these studies agree qualitatively: a single cyclone or anticyclone decreases or increases the Kuroshio transport, respectively, whereas a pair of eddies (also called "dipole eddy") could either strengthen or weaken the Kuroshio, depending on the alignment angle of the two adjacent eddies (Yan et al., 2016). However, the processes governing the evolution during the interactions of mesoscale eddies with the Kuroshio are rarely discussed in the literature. This is largely due to the lack of comprehensive in situ observations combined with the insufficient spatial and temporal resolution of satellite SSH observations, which have the added limitation of only capturing the surface conditions. Therefore, this study takes advantage of the field observations reported in Tsai et al. (2015) and Andres et al. (2017), supplemented with satellite observations, to look into the underlying physical processes during Kuroshio-eddy interactions east of Taiwan with the dynamical interpretations guided by output from semi-idealized, process-oriented numerical simulations.

Tsai et al. (2015) analyzed the correlations between acoustic travel times measured by four pressure-sensor equipped inverted echo sounders (PIESs) at the KTV1 line and satellite sea surface height anomalies (SSHa) east of Taiwan. From the observed linear correlations, they inferred that impinging eddies lead to seesaw-like SSHa and pycnocline depth variations across the Kuroshio. Figure 1 schematically illustrates sea level and isopycnal changes in eddy-Kuroshio interactions hypothesized by Tsai et al. (2015) based on these correlations. Cyclonic eddies weaken sea surface and pycnocline slopes and, in turn, the throughflow transport (Figure 1a), whereas anticyclonic eddies enhance these slopes and transport (Figure 1b) across the Kuroshio at the KTV1 line. A key result from Tsai et al. (2015) is that the spatial range of the direct influence of westward propagating eddies does not cross the Kuroshio's maximum velocity core east of Taiwan (thereby resulting in the seesaw pattern in slope variations spanning this core). This finding warrants further validation with a model for two reasons. First, the four PIESs were relatively widely spaced compared to the Kuroshio width. Second, acoustic travel time is only an indirect measure of thermocline (or pycnocline) displacement. Though this proxy has been validated with historical hydrography from the region (Andres et al., 2017) it is valuable to verify it in the framework of the numerical model as well.

The primary goal of this study is to examine the evolutions in the velocity structure, hydrography, and kinetic and available potential energies during interactions of eddies of both signs with the Kuroshio. To the best of our knowledge, this is the first attempt to examine these evolutions using observations and numerical modeling and a key model result is that arrivals of eddies east of Taiwan can have important remote effects, both in the Luzon Strait/South China Sea and on the East China Sea shelf. A three-dimensional numerical model with simplified forcing (called semi-idealized model hereafter) is adopted to simulate the impinging of an idealized single eddy of both signs on the Kuroshio in numerical experiments with different parameter settings. Results from the simulations are compared with the hydrographic and velocity profiles deduced from PIES data at the KTV1 line (Andres et al., 2017; Mensah et al., 2016), and with satellite altimeter-measured SSH distributed by Archiving, Validation, and Interpretation of Satellite Data in Oceanography (AVISO). The kinematic processes during eddy-Kuroshio interactions are the central focus of the analysis of the observations and model results. Section 2 describes the sources of the observational data used in this study. The numerical model is described in section 3 with model parameter settings and associated model-data validation described in Appendix A, and with the setup of an eddy in the model

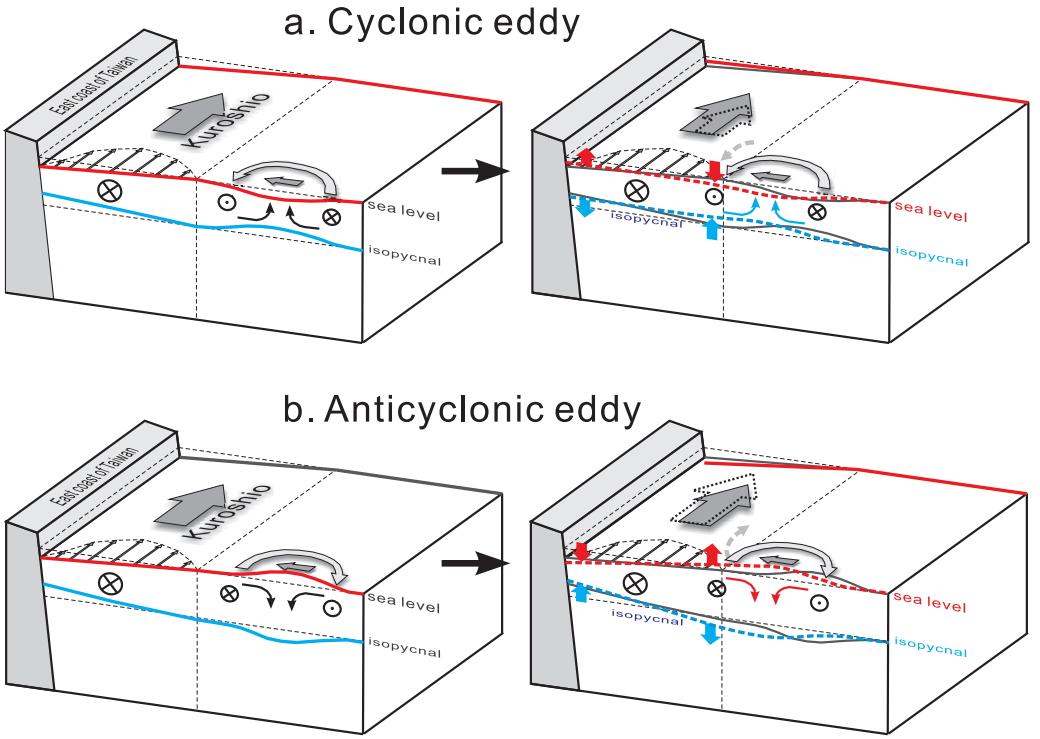

Figure 1. Schematic diagram showing changes in sea level height, isopycnal depth, and the throughflow transport in a fixed section that occur when (a) a cyclone and (b) an anticyclone impinge on the Kuroshio east of Taiwan.

using the Rankine Vortex winds included in Appendix B. Results from numerical experiments are described and discussed in sections 4 and 5, followed by a summary in section 6.

2. Observational Data

An array of PIESs was deployed across the Kuroshio east of Taiwan from November 2012 to October 2014 (Andres et al., 2017; Mensah et al., 2016). PIESs are deployed on the seabed and measure the hourly surface-to-bottom round-trip acoustic travel time, which is a function of the time-varying vertical profiles of temperature and salinity. Acoustic travel time (τ) data obtained from four PIESs deployed at stations P1, P2, P3, and P4 along the KTV1 line (Figure 2b) are used here to examine changes in the hydrographic structure and the Kuroshio transport during eddy-Kuroshio interactions during two periods, from 20 April to 20 June 2013 and from 15 June to 15 August 2014, when eddies were interacting with the Kuroshio. A brief summary of the PIES processing methodology is described here. For further details about PIES data processing, the reader is referred to Tsai et al. (2015), Mensah et al. (2016), and Andres et al. (2017). The PIES raw τ data collected at each instrument's depth were converted to acoustic travel time at the reference depth of 800 dbar (τ_{800}). These τ_{800} time series were then mapped onto a 10 km spaced grid, and the daily mapped data at each grid-cell were converted to profiles of temperature and specific volume anomaly through the use of Gravest Empirical Mode (GEM) lookup tables (Meinen & Watts, 2000; Sun & Watts, 2001; Watts et al., 2001). The velocity shears referenced to 800 dbar were derived from the specific volume anomaly data via the thermal wind relationship. The reference velocity at 800 dbar is time varying and was obtained by calculating the differential of the leveled pressure sensor time series between each instruments (Andres et al., 2017), which was further used to calculate absolute geostrophic velocity profiles across the current. The 800 dbar reference level is selected to be consistent with that used in Tsai et al. (2015), which is also approximately the lower bound of the Kuroshio's poleward velocity. Recent works (Andres et al., 2017; Mensah et al., 2016) demonstrate that the PIES data are particularly suitable for studying the Kuroshio, and good agreement is found between results derived from PIES observations and other platforms, such as moored and lowered acoustic Doppler current profilers (ADCPs) and underwater gliders.

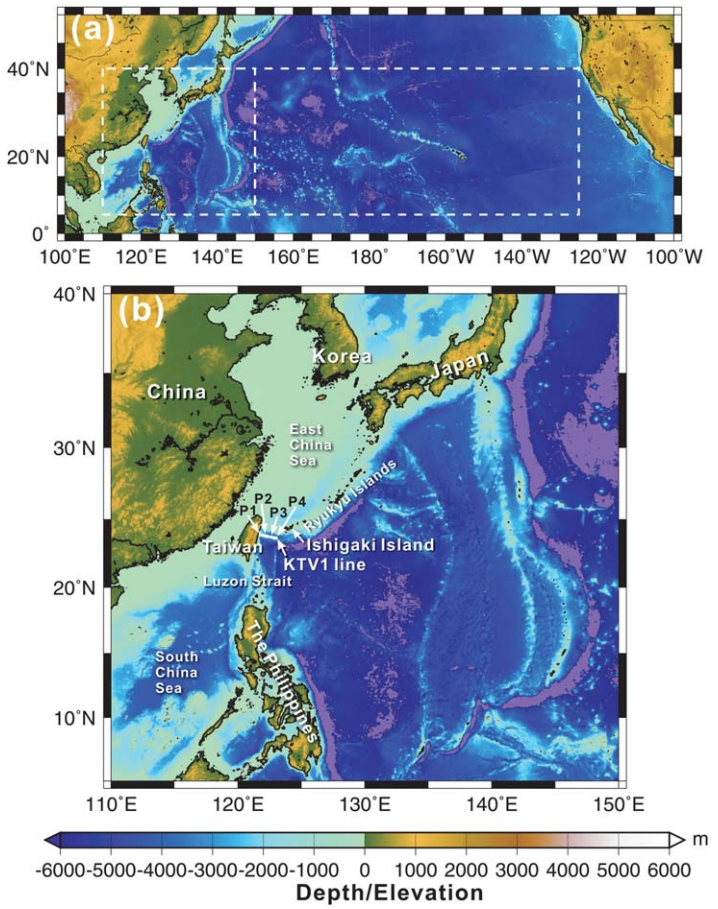

Figure 2. Bathymetry in the North Pacific. (a) Model domain bounded meridionally by 110°E and 125°W, and zonally by 5°N and 40°N, and (b) a close-up of the model domain in 110°E–150°E and 5°N–40°N. The four PIES stations along the KTV1 line east of Taiwan are indicated by P1, P2, P3, and P4.

Fifteen shipboard surveys, conducted aboard R/Vs Ocean Researcher I or V using conductivity-temperature-depth sensors (CTD) and lowered ADCP at eight stations along the KTV1 line, provide hydrography and velocity from the surface to near-bottom in the Kuroshio. Results from the first nine surveys, completed during 16–17 September 2012, 7–8 November 2012, 13–15 November 2012, 25–27 June 2013, 1–2 October 2013, 24–25 December 2013, 8–12 March 2014, 4–6 July 2014, and 10–11 September 2014, have been reported in Jan et al. (2015). The latter six surveys were conducted during the periods of 8–9 November 2014, 4–5 March 2015, 10–11 June 2015, 6–7 September 2015, 6–7 November 2015, and 30 June to 1 July 2016. The shipboard instruments are described in Jan et al. (2015). The ship survey data were processed following the procedures detailed in Jan et al. (2015). The averaged velocity and hydrography obtained from the 15 ship surveys are used here to validate the model results.

The 0.25° gridded, delayed-time satellite sea surface height (SSH) data that merge measurements from all available satellites were downloaded from AVISO via Ssalto/Duacs (http://www.aviso.oceanobs.com/en/data/products.html) to detect mesoscale eddies and to compare with model results. The geostrophic currents derived from SSH are also used to validate the modeled flow field during eddy-Kuroshio interactions.

3. Numerical Model

A three-dimensional numerical model developed from the Princeton Ocean Model (POM) (Blumberg & Mellor, 1987) was adopted to examine variations in the hydrographic and velocity field when mesoscale eddies impinge on the Kuroshio east of Taiwan. The POM is a nonlinear, primitive equation model with Boussinesq and hydrostatic approximations. The governing equations are described in, e.g., Blumberg and Mellor (1987) and are therefore not shown here.

The model domain is bounded by the 110°E and 135°W meridians, and by the 5°N and 40°N parallels, covering the majority of the subtropical North Pacific Ocean (Figure 2). The grid spacing is 0.1° (∼10 km at 24°N) west of 150°E and 0.2° east of 150°E in the zonal direction, and is 0.1° (∼11 km) in the meridional direction. The grid resolution is sufficient to resolve both the width of the Kuroshio, which varies in the observations from 85 to 135 km (Jan et al., 2015), and the mesoscale eddies which are observed to have radii of 120–250 km (Cheng et al., 2017; Tsai et al., 2015; Yang et al., 2013). The vertical axis of the model is the σ-coordinate (Blumberg & Mellor, 1987). There are 32 layers of uneven thickness in the vertical (see Appendix A). For a water depth of 4,000 m, for example, the layer thickness is ∼9–18 m in the upper 109 m, and ∼18 m from 109 to 364 m, which is sufficient to resolve eddy-induced vertical displacements of the pycnocline in the Kuroshio. The construction of the model topography, parameters used in the model, and validations of model-simulated hydrography and circulation are reported in Appendix A. Note that the model does not assimilate observational data to retain the dynamics of the model as much as possible. Since the numerical simulation here is semi-idealized rather than realistic, further fine tuning of the model to fit the observations is not warranted. The modeled circulation at the end of year 5 was used as the initial field for our numerical experiments.

To produce a freely propagating eddy in the model, cyclonic (anticyclonic) wind stresses generated using the Rankine Vortex theory described in Holland (1980) were superimposed on the background winds and then applied to the sea surface to produce a cyclonic (anticyclonic) eddy in the ocean. The calculation of the Rankine Vortex winds and how the winds are applied to the model are described in Appendix B.

In addition to the three-dimensional hydrography and velocity fields, the model also simulated PIES observations at P1, P2, P3, and P4. The sound speed in the modeled hydrographic field was calculated using the formula delineated in Fofonoff and Millard (1983), which is a function of temperature, salinity, and pressure.

Table 1
Parameters Used to Produce the Rankine Vortex Winds for Each Numerical Experiment

	Rankine Vortex wind			Initial eddy center		
Eddy	P_c (hPa)	dP_c (hPa)	R_{max} (km)	Lon. (°E)	Lat. (°N)	Mean ζ/f
CE1	960	48	100	130	18.5	0.248
CE2	980	27	100	130	18.5	0.163
CE3	960	48	100	130	19.5	0.220
AE1	960	48	100	130	23.5	−0.271
AE2	980	27	100	130	23.5	−0.131
AE3	960	48	100	130	24.5	−0.273

Note. P_c is center pressure of the Rankine Vortex wind; dP_c is the pressure drop in the vortex wind center; R_{max} is the radius of maximum wind; Mean ζ/f is the spatially averaged ratio of relative vorticity (ζ) to planetary vorticity (f) in the eddy with a radius of 75 km on day 45. Relative vorticity ζ was derived from the velocity at 50 m depth.

Acoustic travel times referenced to 800 dbar at the four PIES stations were thereby derived from the sound speed, which were stored for comparison with the observed travel times.

To achieve the objective of this study, six numerical experiments with different settings of the initial location, strength, and polarity of the eddy were performed. Each experiment simulated the impingement on the Kuroshio of a westward propagating eddy generated at 130°E. The distance from the initial longitude of an eddy center to the offshore edge of the Kuroshio, which is 6–7 times of the eddy's mean radius ~110 km, is long enough to ensure a free propagation of the model-produced eddy. The initial latitude of an eddy center was chosen in accordance with the impinging latitude, which is defined as the latitude where the western edge of an eddy encounters the offshore side of the Kuroshio. Table 1 lists the parameter settings for the six experiments. Experiments CE1 and AE1 represent interactions of the Kuroshio with a relatively strong cyclonic and anticyclonic eddy, respectively. The impinging latitude was approximately 21.5°N for CE1 and AE1. The Rankine Vortex winds for generating CE2 and AE2 were decreased, and thus the modeled eddies were weaker than CE1 and AE1. CE3 and AE3 are similar to CE1 and AE1, but the impinging latitude of the two eddies is 1° further north than that of CE1 and AE1. Results from the numerical experiments are shown and discussed below.

4. Results

The dependence of eddy-evolution and eddy-Kuroshio interactions on the eddy strength and impinging latitudes are examined. A representative cyclonic and an anticyclonic eddy, which are identified from AVISO SSH and are relatively "clean" in comparison with the other eddies during the PIES observations, impinged on the Kuroshio during 20 April to 20 June 2013 and 15 June to 15 August 2014, respectively. Since the ζ/f ratios of the two eddies (approximately 0.190 and −0.238) are within the range of ζ/f ratio of the modeled eddies, they are chosen here to compare with the model results. Because of the lower temporal and spatial resolution of AVISO SSH compared to that of the model, only four periods during each of the eddy-Kuroshio interactions were selected to represent different stages of the evolution (Figure 3).

4.1. Deformation of the Eddy Shape and Change in Kuroshio Transport

To examine the model results during different stages of an eddy-Kuroshio interaction, Figure 4a shows snapshots of the simulated temperature and velocity at 50 m depth for CE1. The western edge of CE1 impinges on the Kuroshio's eastern flank at ~21.5°N (day 50). The eddy shape remains circular and the maximum velocity is ~0.5 m s^{-1} on day 50. On day 60, the eddy deforms from a circular to an elliptic shape and the southward flow of the eddy and poleward-flowing Kuroshio encounter each other. The eddy continues to deform and part of its outer flows split to the south of the Ryukyu Islands. On day 65, the ellipse is further stretched in the north-northwest and south-southeast directions. The northern part of the stretched CE1 attaches to the Kuroshio and is advected by the Kuroshio through the passage between Taiwan and Ishigaki Island on day 70. The eddy is weakened and cold water in the eddy core is absorbed by the Kuroshio and gradually loses its character. The eddy continues to be destroyed, and a small cold water patch with a diameter ~100 km appears off the northeast coast of Taiwan on day 80. The hydrographic and velocity structure of the eddy are eventually dissipated after day 90. Thereafter, the upstream Kuroshio recovers to its "original" state. The duration of the eddy-Kuroshio interaction is ~40 days. Similar to time evolution of the temperature and velocity in Figure 4a, the cyclonic eddy's characteristic low sea level center and positive ζ/f (Figure 4b) undergo a process of encountering, deforming, elongating, and dissipating the eddy's features. Figure 4 also demonstrates that the eddy CE1 seems to trigger a Kuroshio intrusion into the northern South China Sea forming a pronounced anticyclonic loop current in the Luzon Strait roughly from day 60 to 90. The formation of this anticyclonic loop is attributed to a remote effect of a cyclonic eddy on the Kuroshio in the Luzon Strait. The evolution during the CE1-Kuroshio interaction is consistent with, but more detailed than, the interactions demonstrated in Kuo and Chern (2011) and Kuo et al. (2017). The results reported in Chern and Wang (2005), Kuo and Chern (2011), and Kuo et al. (2017) were indeed produced by a reduced-

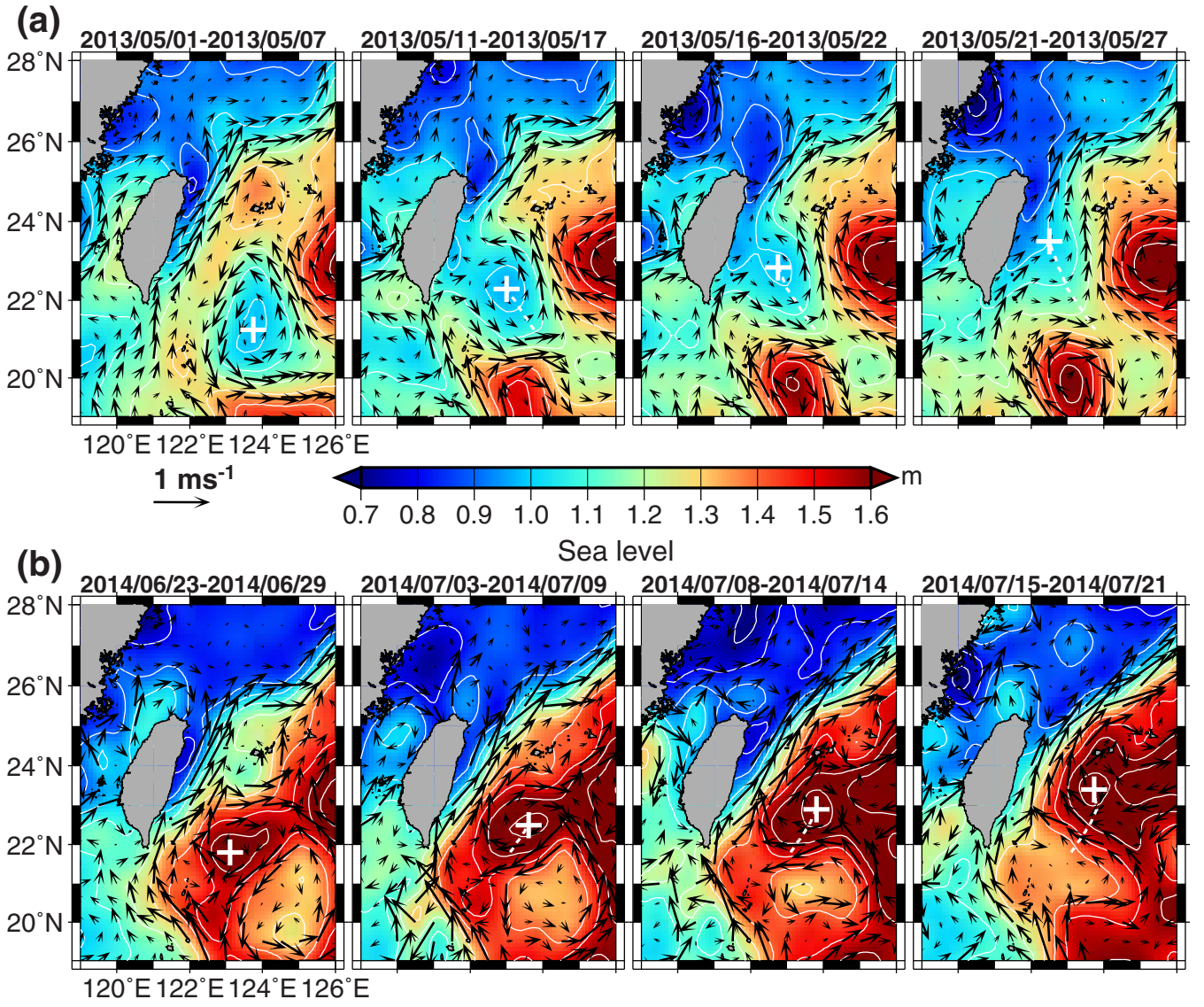

Figure 3. Spatial and temporal evolution of mesoscale eddies detected from AVISO 0.25° gridded, 7 day composite SSH and corresponding geostrophic currents. (a) A cyclonic eddy during composite periods 1–7 May, 11–17 May, 16–22 May, and 21–27 May 2013; (b) an anticyclonic eddy during 23–29 June, 3–9 July, 8–14 July, and 15–21 July 2014. The eddy center is marked by white "+" and the eddy track is indicated by white dashed lines.

gravity primitive equation model with an undisturbed upper layer thickness of 300 m, which cannot simulate the influence from a realistic topography, particularly near the western boundary of their model.

Figures 5a and 5b show the evolution of temperature, velocity, and ζ/f at 50 m depth and sea level at different stages when the anticyclonic eddy AE1 impinges on the Kuroshio. The absolute value of ζ/f is also a measure of the Rossby number. AE1 encounters the Kuroshio at ~21.5°N and is deformed to an elliptic shape with the major axis parallel to the maximum velocity axis of the Kuroshio during the early stages of the interaction (days 50, 60, and 65). As time progresses, the Kuroshio starts to envelop the eddy, leading to the acceleration of the poleward current off the northeast coast of Taiwan (e.g., day 70 in Figure 5a). The eddy further merges with the Kuroshio downstream along the shelf break in the East China Sea after day 90.

Next these modeled evolutions of eddies CE1 and AE1 are compared with satellite altimeter observations of a cyclonic and anticyclonic eddy, respectively, that are identified from AVISO SSH and the SSH gradient-derived geostrophic currents (Figure 3). Note again that the comparison is qualitative because of the idealized nature of our model runs and the low temporal and spatial resolution of altimetry. During a composite

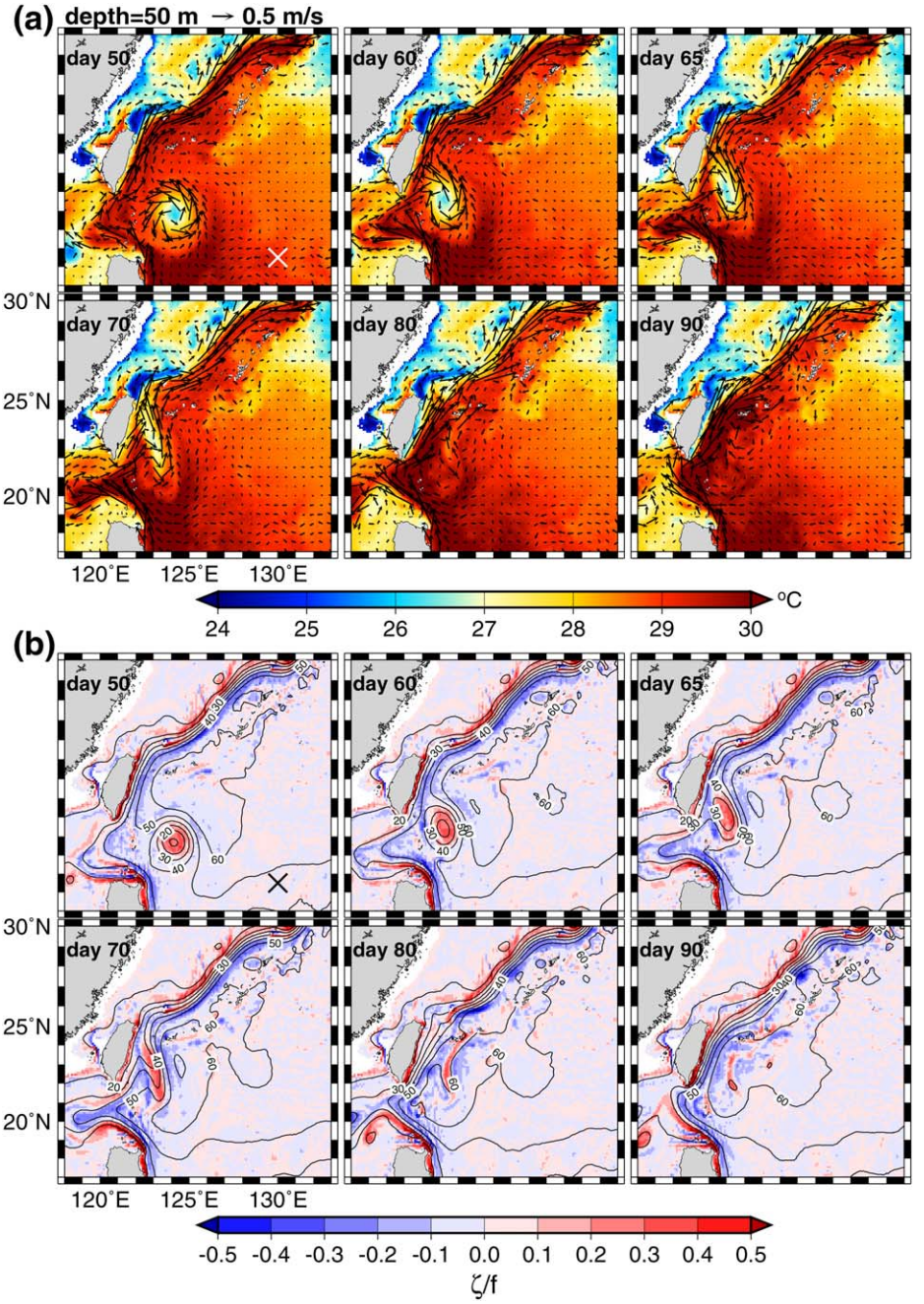

Figure 4. Results of the simulated CE1: (a) 50 m temperature (color shaded) and velocity (arrows) and (b) sea level (contours) and the ratio of relative vorticity (ζ) to planetary vorticity (f) on days 50, 60, 65, 70, 80, and 90. The symbol "×" marks the initial center of the eddy.

period from 1 May 2013 to 7 May 2013, a cyclonic eddy centered at 123.75°E and 21.25°N (white "+" in Figure 3a) starts to approach the eastern flank of the Kuroshio (corresponding qualitatively to day 50 in Figure 4a). This eddy then experiences dissipation and distortion of its shape over the following 20 days. During the interaction, the Kuroshio velocity inferred from the mapped SSH decreases and the current is not as tightly constrained to the east coast of Taiwan. An anticyclonic eddy, marked by white "+" at its center in Figure 3b, encounters the Kuroshio during 23–29 June 2014. The major axis of this elliptic-shape eddy becomes rotated to the direction of the Kuroshio's maximum velocity axis during 8–14 July 2014 (corresponding to day 70 in Figure 5a). The Kuroshio is strengthened during 3–9 July 2014 and 8–14 July 2014. It

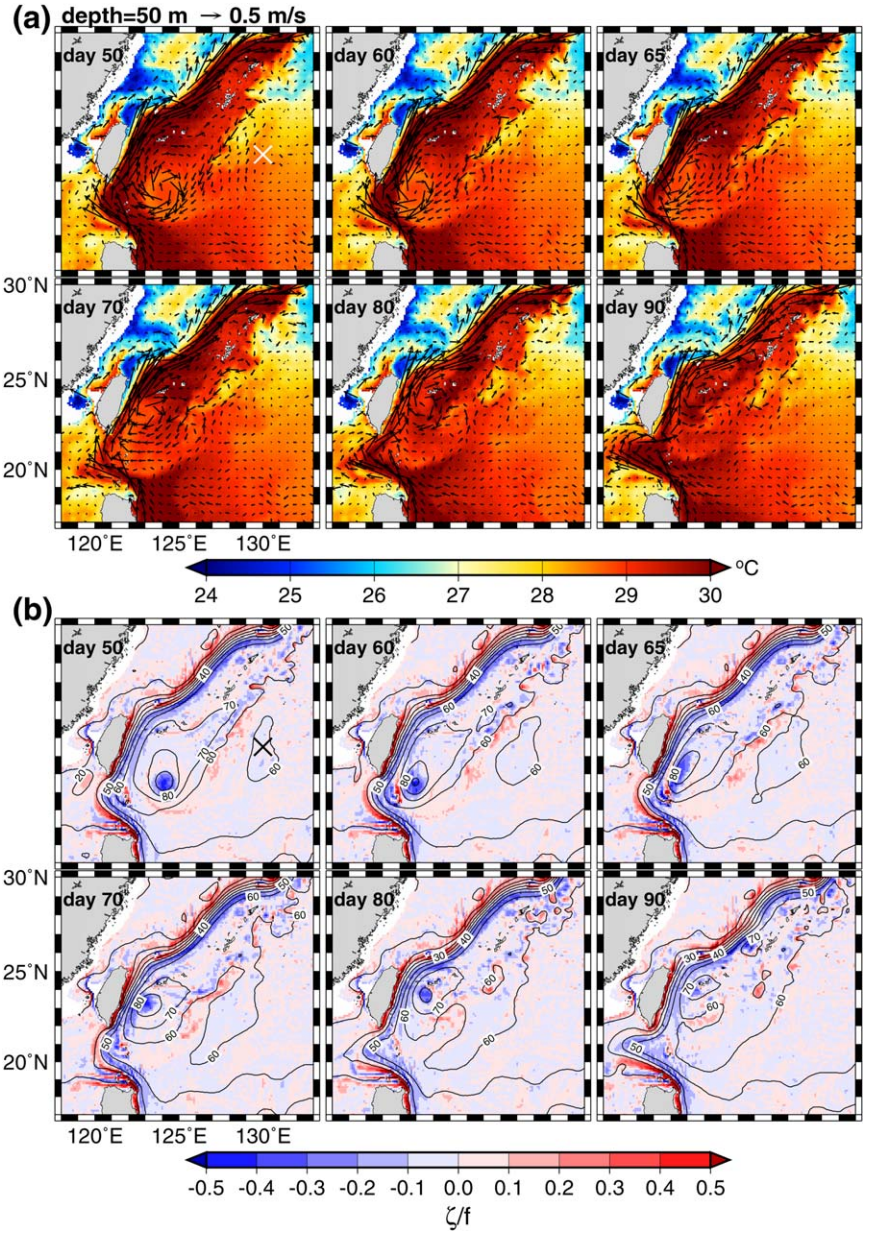

Figure 5. Same as Figure 4, but for the eddy AE1.

should be noted that, in Figure 3, low or high SSH features and the associated eddies are complicated due to multiple arrivals of dipole eddies aligned either in the zonal or meridional directions and, in some cases, even tripole eddies. Regardless of this complexity in the realistic ocean, the model captures the essential features apparent in the satellite SSH field and the associated geostrophic flows. The numerical simulation provides a relatively clean environment for isolating the processes involved in individual eddy-Kuroshio interactions and examining them in more detail than is possible with the surface data from satellites.

For further comparison between model and observations, the throughflow transport at 23.7°N between the grid-cell closest to the coast and 123°E in the model (approximately the KTV1 section), was calculated by integrating over the modeled poleward velocity where $v \geq 0.2$ m s^{-1} in the upper 800 m, which is called the Kuroshio transport hereafter for simplicity. PIES data (referenced to 800 dbar) were also used to calculate the poleward transport through section P1–P4 (KTV1 line) for periods from 20 April 2013 to 20 June 2013

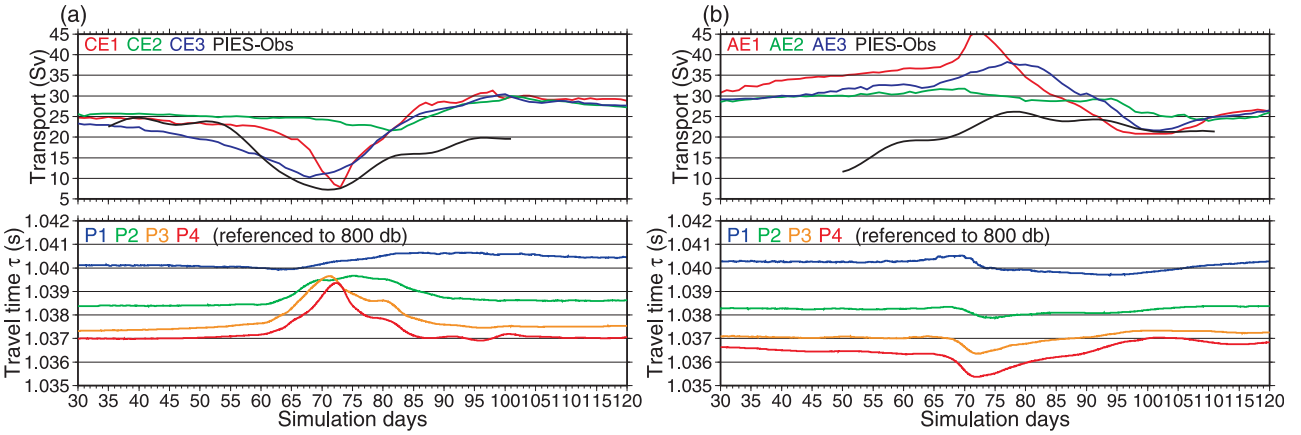

Figure 6. Poleward volume transport through 23.7°N (integrated from 121.7°E to 123°E and from 800 m to the surface with $v \geq 0.2$ m s^{-1}) and model-simulated acoustic travel time (referenced to 800 dbar) at stations P1 through P4 for eddies (a) CE1, CE2, and CE3, and (b) AE1, AE2, and AE3. Black lines represent PIES-data-derived geostrophic flow transport at the same transect for periods (a) from 20 April 2013 to 20 June 2013, corresponding to model days 40–100 in CE1, and (b) from 15 June 2014 to 15 August 2014, corresponding to model days 50–120 in AE1.

(corresponding to days 40–100 in CE1), and from 15 June 2014 to 15 August 2014 (day 50–120 in AE1), covering the two periods of the cyclonic and anticyclonic eddies shown in Figure 3. The transport was calculated using PIES-derived geostrophic currents with $v \geq 0.2$ m s^{-1} in the upper 800 dbar, and was further low-pass filtered to exclude fluctuations with periods shorter than 14 d. The detailed procedure for PIES data processing is given in Mensah et al. (2016) and Andres et al. (2017). Figure 6 shows observed and modeled volume transport (top plots) and acoustic travel time (lower panels) from model day 30 to 120. Not surprisingly, the transport in the 23.7°N section decreases (increases) when a single cyclonic (anticyclonic) eddy impinges on the Kuroshio in both the model runs and observations. This consistency in the modeled and observed Kuroshio transport variability at the fixed KTV1 section, ~ -20 Sv (1 Sv $= 10^6$ m^3 s^{-1}) during the impingement of cyclones and $\sim$15 Sv during anticyclones, lends further support to our use of the model as an analysis tool to examine the evolution of hydrography and velocity structure during eddy-Kuroshio interactions east of Taiwan.

As a final comparison between model and observations, acoustic travel times (which are a proxy for isopycnal displacements) are considered. Model-simulated acoustic travel times referenced to 800 dbar at the four PIES stations (bottom plots in Figure 6) suggest that the water column temperature decreases and the travel time increases, particularly at stations P3 and P4 when CE1 impinges on the offshore side of the Kuroshio. In contrast, variations in temperature and the associated travel time are reversed during the AE1-Kuroshio interaction. The variations in the acoustic travel time and throughflow transport in the 23.7°N section are consistent with the hypothesized process of eddy-Kuroshio interaction of Tsai et al. (2015) shown schematically in Figure 1.

With the good correspondence established between modeled and observation-inferred SSH signals, transport variations, and isotherm displacements, we next use the model to examine details of the evolution of eddy-Kuroshio interactions.

4.2. Variations in the Sea Level and Isopycnal Depth

Associated with the eddies shown in Figures 4 and 5, the vertical structures of hydrography and velocity along a section approximately across the eddy center on simulation days 50, 60, 70, and 80 are illustrated in Figures 7 and 8 for CE1 and AE1, respectively. Changes in sea level and isopycnal depths lead to seesaw-like patterns across the Kuroshio, consistent with those suggested by the observations reported in Tsai et al. (2015). The sea level deepens (heaves) and pycnocline heaves (deepens) on the offshore (onshore) side of the Kuroshio when the eddy CE1 encounters the Kuroshio (Figures 7b and 7c). The vertical movement of sea level and isopycnal is reversed when AE1 impinges on the Kuroshio (Figures 8b and 8c).

The eddy's velocity and the associated vertical displacements of isotherms/isopycnals extend to 800–1,000 m as CE1's western edge encounters the Kuroshio. The southward velocity in the western half of CE1

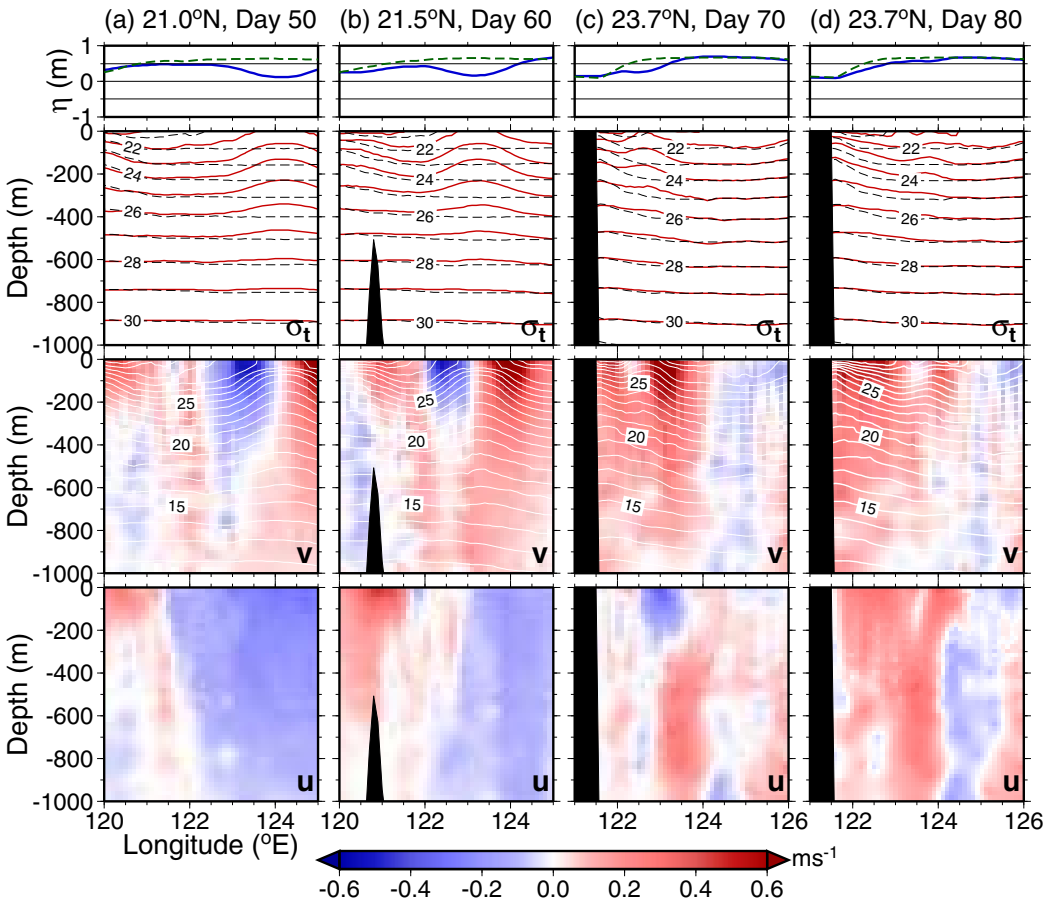

Figure 7. Snapshots of zonal sea level (blue lines) and vertical profiles of isopycnal depths (red dashed contours in σ_t), velocity (v and u in colors), and isotherm (white contours in °C) in the eddy CE1 at (a) 21.0°N and day 50, (b) 21.5°N and day 60, (c) 23.7°N and day 70, and (c) 23.7°N and day 80. The sea level and density (σ_t) in an accompanying model run without eddies are plotted, respectively, in green and black dashed lines.

weakens below 300 m as the eddy-Kuroshio interaction progresses (Figure 7b), and eventually loses its character (Figures 7c and 7d). The northward velocity profiles show two velocity maximum cores in the Kuroshio (Figures 6b and 6c), which is consistent with some of the ship observations shown in Jan et al. (2015) and discussed in a dynamic framework in Yang et al. (2015). At the section at 23.7°N (KTV1 line), the westward velocity becomes sizable in the upper 300 m east of the Kuroshio (Figure 7c) due to the north-northwestward elongation of CE1 when the eastern half of CE1 approaches the offshore Kuroshio on day 70 (Figure 4a). Meanwhile, the zonal velocity below 300 m is opposite to that in the upper 300 m. This westward velocity in the upper 300 m weakens quickly when the eddy is engulfed by the Kuroshio (Figure 7d).

During the impingement of AE1 onto the Kuroshio, the northward velocity in the western half of AE1 is strengthened in the early stages of the interaction (Figure 8b). As the AE1-Kuroshio interaction proceeds, the northward velocity in AE1's western half merges with the Kuroshio, leading to a faster and wider "Kuroshio" adjacent to the east coast of Taiwan (Figures 8c and 8d). The zonal velocity shows considerable confluence in the upper 300 m at ~122.5°E (cf. Figure 8c with day 70 in Figure 5a).

5. Discussion

The physical factors that determine the changes of hydrography and transport in the Kuroshio when mesoscale eddies impinge upon it comprise the polarity, spatial scale, nonlinearity, impinging location of the eddy, and even the alignment and arrival sequence of dipole eddies (e.g., Yan et al., 2016). It is emphasized that the present study is designated to examine the effects only of an eddy's strength and impinging

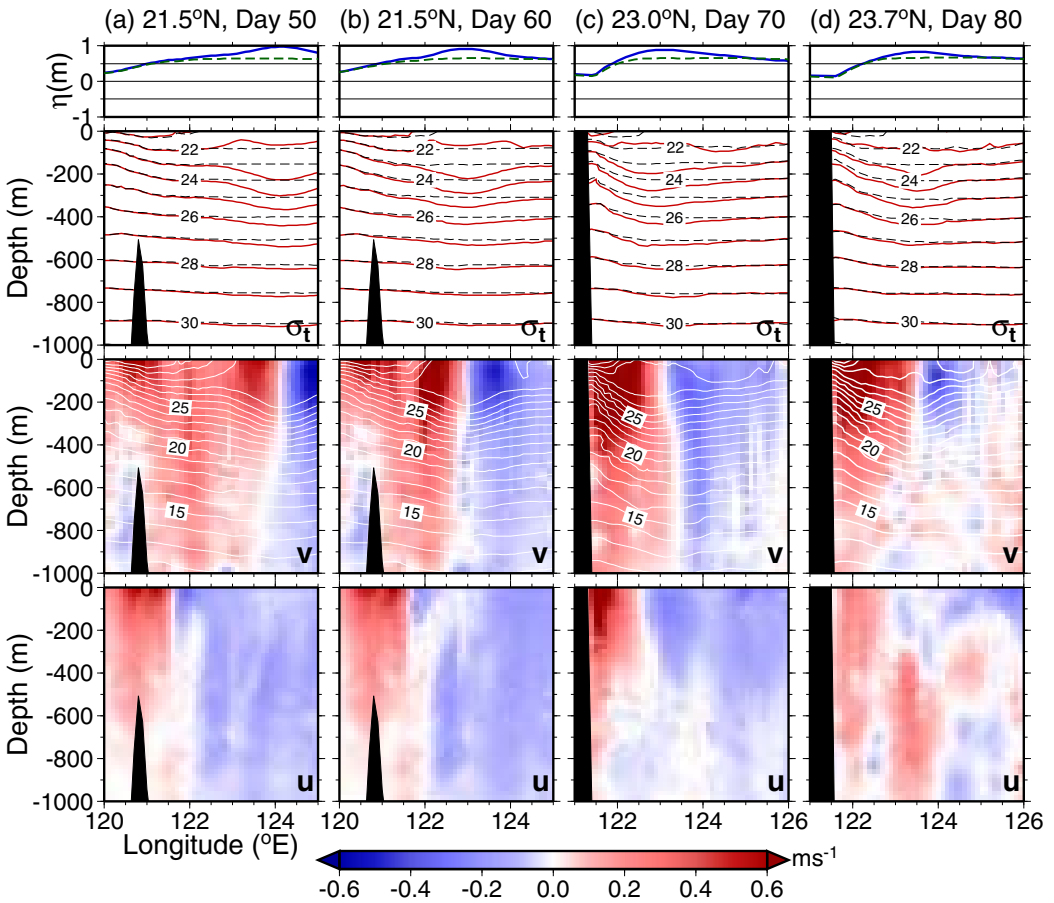

Figure 8. Similar to Figure 7 but for the eddy AE1 at (a) 21.5°N and day 50, (b) 21.5°N and day 60, (c) 23.0°N and day 70, and (c) 23.7°N and day 80.

latitude on the Kuroshio and, importantly, to investigate physical processes during the eddy-Kuroshio interaction.

To quantify eddy strength, the eddy kinetic energy (KE_e) and available potential energy (APE) were calculated. The KE_e was calculated as:

$$KE_e = \frac{1}{2}\rho_0(u_e^2 + v_e^2 + w_e^2) \tag{1}$$

where the velocity components of the eddy field (u_e, v_e, w_e) are obtained by subtracting the concurrent velocity field of a similar model run, without eddy influence ($\vec{u}_{no}$) from the velocity of each numerical experiment ($\vec{u}$), i.e., $\vec{u}_e(x,y,z,t) = \vec{u}(x,y,z,t) - \vec{u}_{no}(x,y,z,t)$. The APE was calculated as:

$$APE = \frac{1}{2}\frac{g^2\rho'^2}{\rho_0 N^2} \tag{2}$$

where g is the gravitational acceleration, ρ' is the perturbation density obtained by $\rho'(x,y,z,t) = \rho(x,y,z,t) - \rho_{no}(x,y,z,t)$ (ρ_{no} is the density in the model run without eddy influence), and N is the buoyancy frequency obtained from $N^2 = -\frac{g}{\rho_0}\frac{\partial\rho}{\partial z}$. To calculate the total energy in an eddy, KE_e and APE were integrated from 800 m to the surface in the vertical, and over the eddy area in the horizontal. The boundary for the horizontal integration in the eddy was set to be where the relative vorticity changes sign from that of the eddy. Figures 9 and 10 demonstrate depth-integrated KE_e and APE for cyclonic and anticyclonic eddies, respectively, on day 65 when these eddies begin to encounter the offshore side of the Kuroshio. The volume-integrated KE_e and APE for each experiment on day 45 and 65 are listed in Table 2. The energy on day 45 is regarded as the "incident" condition before the eddy "hits" the Kuroshio. The evolutions of the KE_e

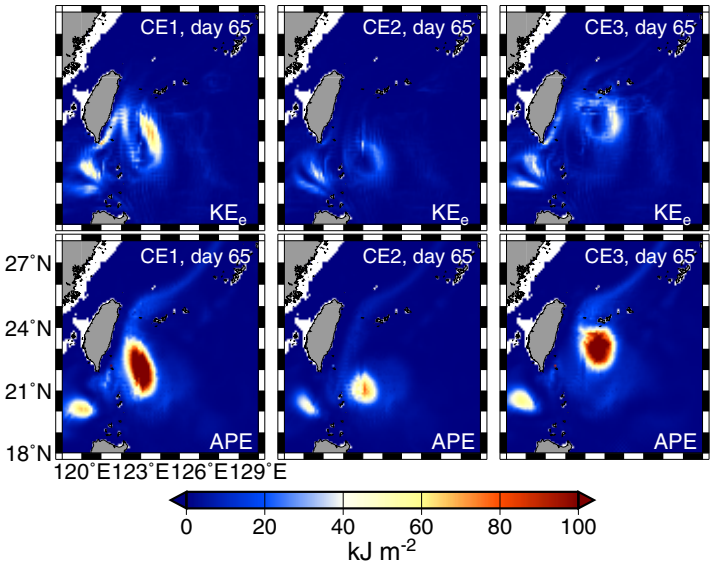

Figure 9. Upper 800 m depth-integrated KE_e and *APE* for the eddies CE1, CE2, and CE3 on day 65.

and *APE* shown in Figures 9 and 10 are the basis for the discussion of the influences of an eddy's strength and impinging latitude on the eddy-Kuroshio interaction.

5.1. Influence of Eddy Strength

The KE_e and *APE* in the modeled eddies are of the same order, 10^{15} J (Table 2), as those of mesoscale eddies in the Subtropical Countercurrent estimated by Ramp et al. (2017). The total energy of the weaker eddy CE2 (which is also smaller in diameter than CE1) is 34.2% of that of CE1 on day 45 (Table 2). The interaction of CE2 and the Kuroshio is delayed by about 10 days compared with the interaction of CE1 and the Kuroshio, due to the smaller size of both the velocity structure and effective energy area of CE2 compared to CE1 (Figure 9). Despite this difference, the evolution of the eddy's shape is qualitatively consistent with that of CE1, as demonstrated in Figure 4a. This weak eddy is elongated meridionally by the Kuroshio east of Taiwan; the eastern half of the eddy is merged into the Kuroshio through the channel between the northeast coast of Taiwan and Ishigaki Island, and is thereafter absorbed and dissipated in the Kuroshio in the southern East China Sea. The APE/KE_e ratio for the strong eddy CE1 on days 45 and 65 remains similar over time (3.40 versus 3.10 in Table 2), but for the weak eddy CE2 this ratio increases from 2.78 on day 45 to 4.31 on day 65. The latter result suggests that KE_e decreases faster than *APE* from day 45 to the early stage of the eddy-Kuroshio interaction (−65.5% versus −46.4%).

For a weaker anticyclonic eddy AE2 with only 20.4% of the total energy of AE1 on day 45 (Table 2), the eddy's velocity structure and energy decay more quickly than AE1 does (Figure 10) after encountering the offshore Kuroshio at a similar impinging latitude to that of AE1. The KE_e/APE ratio is 1.61 (day 45) and 2.16 (day 65) for AE1 and 1.76 (day 45) and 3.08 (day 65) for AE2. Similar to the decay of CE2, the KE_e of AE2 decreases more rapidly (−62.4%) than the *APE* decreases (−34.4%). In terms of energetics (Figure 10), the interaction of the Kuroshio with AE2 is much weaker than with AE1.

5.2. Influence of Impinging Latitude

Figure 11 shows temperature, velocity, sea level, and ζ/f ratio at 50 m depth for CE3 on days 70, 80, and 90. The evolution of the cyclonic eddy CE3, which is similar to CE1 in strength but impinges on the Kuroshio ~1° further north than does CE1, differs considerably from the velocity and vorticity evolutions in CE1 (cf. Figure 4). Changes in CE3, particularly during the latter half of the eddy-Kuroshio interaction period (i.e., after day 70), show that CE3 is split by Ishigaki Island as it is dragged by the Kuroshio to the north (day 70 and 80 in Figure 11). The northwestern half of the eddy is absorbed by the Kuroshio through the channel between Taiwan and Ishigaki Island, leading to a pronounced Kuroshio intrusion onto the continental shelf in the southern East China Sea (e.g., day 80 in Figures 4a and 11a), compared with the remote effect caused by anticyclonic eddies here. This type of Kuroshio intrusion, which occurs in both CE1 and CE3, has been observed by drifters and reported in Vélez-Belchí et al. (2013). Importantly, the present study finds the dynamic link between the Kuroshio intrusion northeast of Taiwan and the impingement of cyclonic eddies east of Taiwan. The relationship between the Kuroshio intrusion onto the East China Sea shelf and the polarity of the impinging eddy observed from our model results is consistent with the results deduced from the laboratory experiments reported in Andres and Cenedese (2013). Their laboratory experiments suggest that the impinging cyclones rather than

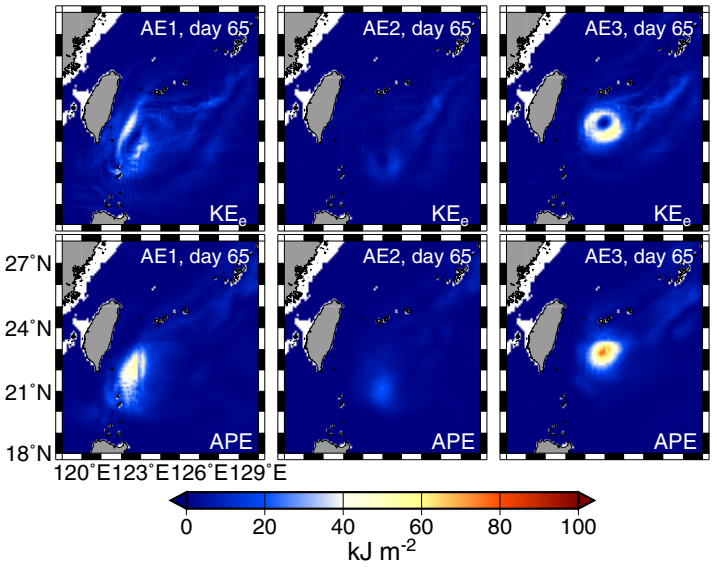

Figure 10. Same as Figure 9 but for the eddies AE1, AE2, and AE3.

Table 2
Volume-Integrated Eddy KE_e and APE for Each Experiment on Day 45 and 65

Exp.	KE_e (10^{15} J)	APE (10^{15} J)	KE_e+APE (10^{15} J)	APE/KE_e
Day 45				
CE1	1.418	4.823	6.241	3.40
CE2	0.565	1.568	2.133	2.78
CE3	1.047	3.685	4.732	3.52
AE1	0.994	1.517	2.511	1.61
AE2	0.186	0.326	0.512	1.76
AE3	0.936	1.511	2.447	1.61
Day 65				
CE1	0.993	3.071	4.064	3.10
CE2	0.195	0.840	1.035	4.31
CE3	0.530	2.325	2.855	4.39
AE1	0.318	0.688	1.006	2.16
AE2	0.070	0.214	0.284	3.08
AE3	0.798	0.992	1.790	1.24

anticyclones seem to force the on shelf flow along an island, which is analogous to the pattern of the intrusion flow off northeastern Taiwan. The southeastern half of the eddy, on the other hand, retains its relative vorticity signature as it drifts northeastward along the southeastern side of the Ryukyu Islands, which could affect the variation in the Ryukyu Current as that reported in Yuan et al. (1998). Because the impinging latitude of CE3 is closer to 23.7°N than is CE1's impinging latitude, the Kuroshio transport through 23.7°N is affected by CE3 about 15 days earlier than by CE1 (Figure 6a). Table 2 suggests that the APE/KE_e ratio increases from 3.52 on day 45 to 4.39 on day 65; the total energy decreases by 39.7% from day 45 to 65, which is larger than the decrease for CE1 (∼34.9%).

The evolution of velocity, hydrography, and energy in AE3 differs from that of AE1 shown in Figures 5 and 10 and Table 2 primarily during the early half of the eddy-Kuroshio interaction, i.e., during days 50–70. Figure 12 further depicts the hydrography, sea level, and ζ/f ratio at 50 m for AE3 on day 50, 60, and 65. Comparing Figures 5a and 12a, AE1 is deformed from a circular to an elliptical shape, with the major axis oriented along the Kuroshio axis, particularly on day 65; while AE3 is slightly deformed to an elliptical shape with the major axis in the zonal direction on day 50, but returns to a circular shape between day 60 and 80. This difference is easily seen in changes in eddy's relative vorticity in Figures 5b and 12b, and in depth-integrated KE_e and APE in Figure 10. The total energy decrease from day 45 to 65 in AE1 is −59.9%, which is larger than that in AE3 (−26.8%). Presumably, the Luzon Strait and the Ryukyu Islands contribute to the difference in the evolution of AE1 and AE3. As AE1 encounters the Kuroshio, westward flows in the southern edge of the eddy push the Kuroshio to form an anticyclonic loop in the Luzon Strait, as the northwestern half of a cyclonic eddy that

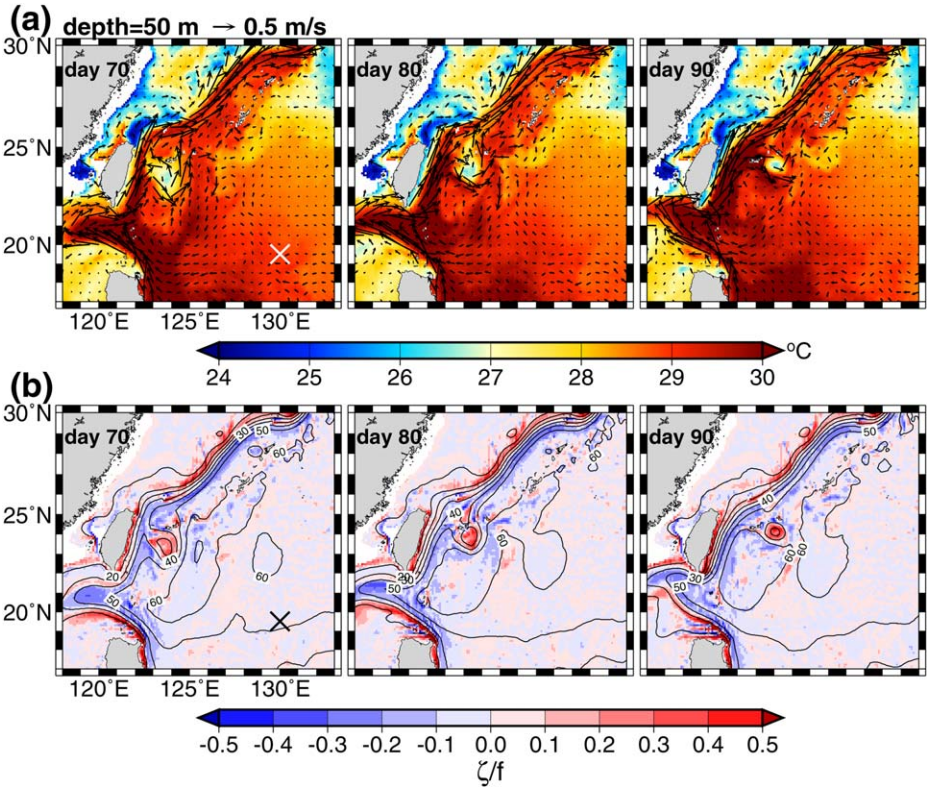

Figure 11. Results of the simulated eddy CE3 at 50 m: (a) temperature (colored) and velocity (arrows) and (b) sea level (contours) and ζ/f ratio on day 70, 80, and 90. Symbol "×" marks the initial center location of the eddy.

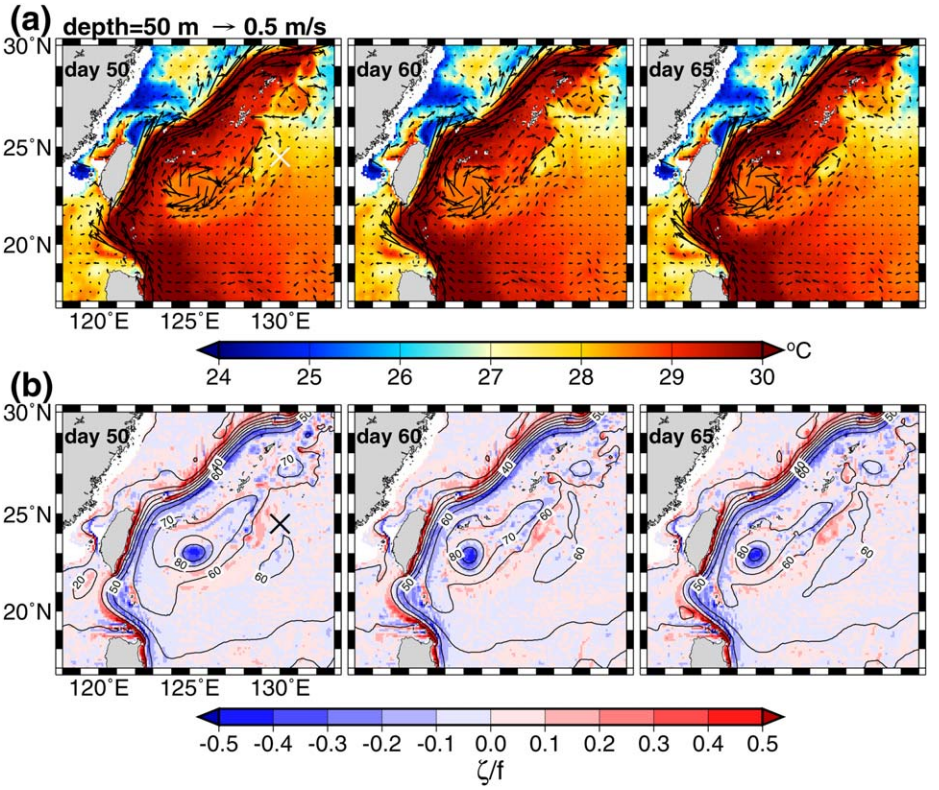

Figure 12. Similar to Figure 11 but for the eddy AE3 on day 50, 60, and 65.

approaches the offshore side of the Kuroshio does (Figure 4). This type of anticyclonic eddy-induced Kuroshio intrusion is consistent with the AVISO SSH and the associated absolute geostrophic current shown in the Figure 1 in Kuo et al. (2017). Concurrently, the western edge of AE1 is driven by the offshore edge of the Kuroshio for a long distance and time from the east of Luzon Strait to the southern boundary of the Ryukyu Islands, which elongates the eddy in the meridional direction. During the evolution of AE3, the Ryukyu Islands behave as a barrier confining the northward movement of the eddy when encountering the Kuroshio. The eddy shape is therefore distorted. The southern edge of the eddy is entrained by the Kuroshio, and the westward eddy flows are partially blocked by the southeast coast of Taiwan as the eddy-Kuroshio interaction evolves, which deforms the eddy to return to a circular shape. A portion of westward flows in the southern edge of the eddy still push the Kuroshio axis westward to loop across the Luzon Strait.

5.3. Kinematics during the Eddy-Kuroshio Interaction

The analysis of the physical processes during the evolution of the eddy-Kuroshio is the primary objective of this study. The physical quantities such as velocities, pycnocline depths, relative vorticity, and kinetic energy obtained from the model results in the 23.7°N section were divided by their maximum absolute value in the spatial range from 121.7°E to 126°E, and temporal range from day 40 (50) to 100 (110) for cyclonic (anticyclonic) eddies. This calculation yields nondimensional (or "normalized") ratios which are compared with the corresponding values obtained from the satellite and concurrent PIES observations of the two eddies shown in Figure 3. Note that the velocity derived from the PIES data is only the meridional component. Anomalies of these physical quantities in the observations were obtained by subtracting the time mean of the data from the raw observations during the observational period. In the modeled field during the period qualitatively the same as the period of the satellite/PIES observations of the two eddies, anomalies of these physical quantities were obtained by subtracting the modeled field without eddy from that with the eddy influence. We used the results derived from the modeled eddies CE1 and AE1 for validation of the model through comparison with the results calculated from the satellite/PIES observations, because the evolution of these two eddies during the eddy-Kuroshio interaction is more consistent with the observations than are

the other model runs. According to the significance of the vertical variation in the isopycnals, isotherms, and velocity in Figures 7 and 8, the comparison is concentrated on the variability in the upper 400 m.

Figure 13 shows the temporal and spatial variation of the normalized anomaly in the hydrography and flow field calculated from satellite/PIES observations from 20 April 2013 to 20 June 2013 (corresponding to day 0–60 in Figure 13a) at the KTV1 line (~23.75°N), and modeled eddy CE1 at 23.7°N (Figure 13b) during the eddy-Kuroshio interaction. The normalized AVISO SSHa in Figure 13a shows a westward propagation of positive SSHa before the arrival of the maximum negative SSHa (indicative of a cyclonic eddy), which reached 123°E on day 15. After about 30 days under the influence of this cyclonic eddy in the section, an anticyclonic eddy with positive SSHa impinged on the Kuroshio on approximately day 45, suggesting the complicated interaction between the Kuroshio and multiple eddies of both signs in the real ocean east of Taiwan. Despite the complexity, the observations and model comparison is focused on day 10–45 (Figure 13a), which qualitatively corresponds to model day 50–85 (Figure 13b). As the cyclonic eddy approached 123°E (Figure 13a), the upper 400 m depth-integrated poleward velocity V_{400} began to decrease (n $V'_{400} < 0$ in Figure 13a) and the negative poleward velocity anomaly V'_{400} propagated shoreward (westward) from the offshore station P4 (123°E) to P1 near the coast at a speed of ~0.106 m s^{-1} during the early stage of the eddy-Kuroshio interaction (day 18–30 in Figure 13a). The V'_{400} further propagated eastward from the vicinity of the offshore station P3 at a speed of ~0.072 m s^{-1} on day 23, and toward the east from the middle location between the onshore stations P1 and P2 at ~0.085 m s^{-1} on day 28, forming a dual eastward propagation of V'_{400} after the middle stage in the eddy-Kuroshio interaction. The eastward propagation of V'_{400} is presumably due to the eastward flow in the southern edge of the eddy, and the reflection that occurred as the westward-propagating eddy influence hits the east coast of Taiwan. The volume transport anomaly Q' (calculated with the limit of poleward velocity $v \geq 0.2$ m s^{-1} in the upper 800 m) and the upper 400 m

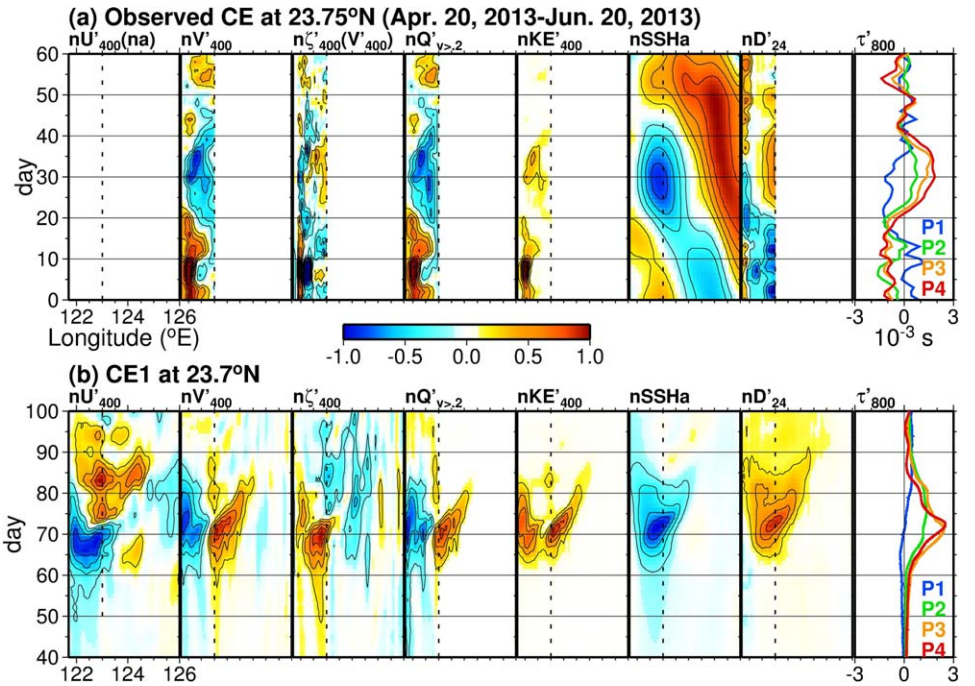

Figure 13. Temporal and spatial (time vs. longitude) variation of the normalized anomaly in the hydrography and flow field calculated from (a) satellite/PIES observations from 20 April 2013 to 20 June 2013 (corresponding to day 0 through 60) at the KTV1 line (~23.75°N) and (b) the modeled eddy CE1 at 23.7°N during the eddy-Kuroshio interaction. n U'_{400} and nV'_{400} are normalized anomalies for the upper 400 m depth-integrated velocity (U'_{400}, V'_{400}). nζ'_{400} is normalized relative vorticity anomaly (calculated from U'_{400} and V'_{400}) anomaly, and KE'_{400} is normalized anomaly of the upper 400 m depth-integrated kinetic energy. nSSHa and nD'_{24} are normalized anomalies for SSH and isopycnal (σ_t=24 kg m^{-3}) depth. nQ' is normalized volume transport anomaly. The transport was integrated with the limit of poleward velocity $v \geq$0.2 m s^{-1} in the upper 800 m in this section. τ'_{800} is the time series of acoustic travel time anomaly (referenced to 800 db). Each variable except τ'_{800} was divided by the maximum absolute value within each panel, so as to become a normalized quantity between −1 and 1. The contour interval is 0.2 and the dashed line indicates 123°E. "na" means not available.

depth-integrated kinetic energy anomaly KE'_{400} (Figure 13a) show similar evolution patterns to that of the V'_{400}. The relative vorticity decreased and propagated shoreward as a narrow strip with negative values from day 15 to 25, and then turned eastward from day 30. The anomaly in the relative vorticity ζ'_{400} (calculated from V_{400}) at the offshore stations P3 and P4 turned positive during day 25 and 40. Subsequently, the pycnocline depth anomaly D'_{24}, which is defined as the deviation of the initial depth of $\sigma_t = 24$ kg m^{-3}, became positive (negative) on the offshore (onshore) side of the Kuroshio, indicating heaving (deepening) of the pycnocline from days 22 to 35. These characteristics of anomalies are consistent with the hypothetical processes illustrated in Figure 1a.

The velocity and hydrographic anomalies during the CE1-Kuroshio interaction from day 55 to 85 (Figure 13b) qualitatively resemble the characteristics obtained from the observations (Figure 13a). The dual eastward propagation of V'_{400} begins on day 68 (Figure 13b) with a propagation speed of 0.076 m s^{-1} from the maximum velocity axis of the Kuroshio, and 0.102 m s^{-1} from the onshore side of the Kuroshio to the east. The model further provides the evolution of the zonal velocity anomaly U'_{400}, which is not obtained from the PIES observations. The westward velocity on the northern edge of the eddy starts to significantly affect the Kuroshio on day 60 (cf. day 60 in Figure 4a). From day 65, the signal of negative U'_{400} propagates from the Kuroshio's maximum velocity axis toward both the west and the east. From day 73, the eastward flow in the southwestern portion of the distorted eddy results in positive U'_{400} on the offshore side of the Kuroshio. Model results further suggest that the eastern portion of the eddy causes positive V'_{400}, Q', and KE'_{400}, which propagate from the offshore edge of the Kuroshio (~123°E) to the east at a speed of 0.146 m s^{-1}. The decrease of SSH and heaving of the isopycnal depth on the offshore side of the Kuroshio lag behind the change in the velocity by 2–3 days. The variations in the modeled τ'_{800} at the four PIES stations (right plot in Figure 13b) agree with the observations (right plot in Figure 13a). Summarizing, both observations and the numerical simulation suggest that, when a cyclonic eddy impinges on the Kuroshio, U'_{400} is likely affected first, followed subsequently by V'_{400}, ζ'_{400}, Q', KE'_{400}, SSHa, and finally D'_{24}.

Figure 14 depicts the comparison of these anomalies in the hydrography and velocity field between the observed anticyclonic eddy (Figure 14a) and the modeled eddy AE1 (Figure 14b). During the period of an early eddy-Kuroshio interaction (day 15 in Figure 14a), V'_{400} and the associated Q' increase and ζ'_{400}

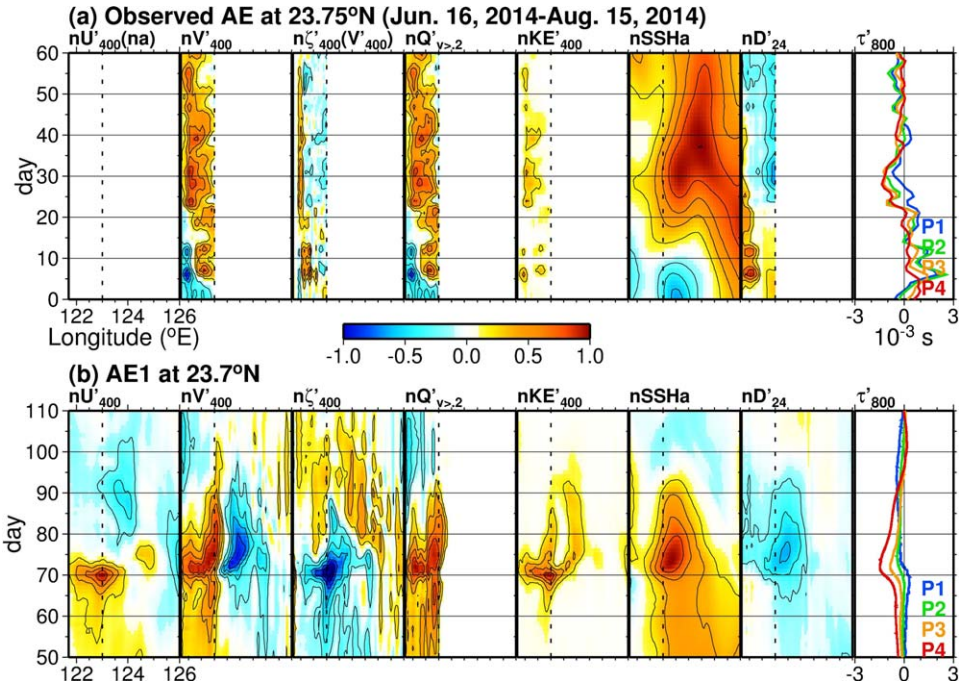

Figure 14. Same as Figure 13, but for (a) satellite/PIES observations from 15 June 2014 to 15 August 2014 (corresponding to day 0–60) and (b) the modeled eddy AE1 (from the simulation day 50–110).

becomes negative prior to the heaving of SSH and deepening of the isopycnal depth on the offshore side of the Kuroshio. The changes in the SSHa and D'_{24} slope are consistent with the evolution during the interaction of an anticyclonic eddy and the Kuroshio schematically depicted in Figure 1b. Figure 14b suggests that, before the maximum interaction approximately on day 70, eastward currents in the northern half of the eddy AE1 lead to positive U'_{400} on the offshore side of the Kuroshio. The poleward flows in the western half of the eddy strengthen the current on the offshore side of the Kuroshio as indicated by positive V'_{400} during days 60 and 90 (Figure 14b). The SSHa and D'_{24} peak east of the Kuroshio's eastern flank on day ~72 and propagate toward both the east and the west (Figure 14b), which are consistent with the variation in the AVISO SSHa (Figure 14a).

Similar to the CE1-Kuroshio interaction, the sequence for the changes in the hydrography and velocity during the AE1-Kuroshio interaction is velocity, SSH, and hydrographic field. The evolution suggests that the increase (decrease) of poleward velocity strengthens (weakens) the SSH and pycnocline slopes across the Kuroshio under the constraint of geostrophic balance; the subsequent approach of the eddy center to the offshore edge of the Kuroshio enhances the seesaw-like variation in both the SSH and pycnocline slopes and results in the change of the Kuroshio transport.

6. Summary

Using PIES and satellite observations interpreted in the context of semi-idealized numerical simulations, this study examined the evolution of interactions of quasi-geostrophic, mesoscale eddies, and the Kuroshio. When an eddy of either sign impinges on the Kuroshio within latitudes 21.5°N–22.5°N east of Taiwan, changes in the velocity and volume transport in the Kuroshio at 23.7°N (KTV1 section) occur first, followed by opposite vertical displacements in the SSH and isopycnal, primarily on the offshore side of the Kuroshio. This, in turn, leads to seesaw-like variations in the SSH and isopycnal slopes across the Kuroshio. The analysis based on both PIES observations and numerical experiments of this study validates the processes hypothetized by Tsai et al. (2015) and illustrated in Figure 1. During the eddy-Kuroshio interaction, both cyclonic and anticyclonic eddies are deformed from circular to elliptical shape; the major axis of the ellipse is in the northeast and southwest directions for cyclones and parallel to the maximum velocity axis of the Kuroshio for anticyclones. The eddies are eventually dissipated and absorbed by the Kuroshio along the continental shelf break in the East China Sea, or partly split to the southeast of the Ryukyu Islands, depending on the impinging latitude, eddy strength and size, and dissipated eventually as well.

The model results also demonstrate the influence of the Luzon Strait, the Ryukyu Islands, and the east coast of Taiwan on the fate of eddies that impinge on the Kuroshio at different latitudes, through processes which are not resolved by Chern and Wang (2005) and Kuo and Chern (2011) due to the lack of realistic topography and the setting of oversimplified western boundary in their model. When a cyclonic eddy encounters the Kuroshio north of 22.5°N, the southwestern end of the Ryukyu Islands splits the eddy to be partly absorbed by the Kuroshio off northeastern Taiwan, and partly separated to become a small, isolated cyclonic eddy south of Ishigaki Island. The former process triggers the Kuroshio intrusion into the southern East China Sea, which explains the dynamics for the Kuroshio intrusion flow observed by drifters off northeastern Taiwan (Vélez-Belchí et al., 2013). The latter process seems to modify the Ryukyu Current off the southeastern coast of the Ryukyu Islands (Yuan et al., 1998). It is also noticed that, when the western edge of a strong cyclonic eddy approaches the offshore side of the Kuroshio, a westward intrusion of the Kuroshio is induced in the Luzon Strait forming a remarkable loop current in the northeastern South China Sea. When a strong anticyclonic eddy encounters the Kuroshio south of 22.5°N, the onshore flow in the southern half of the eddy pushes the Kuroshio to the west in the Luzon Strait, causing an anticyclonic loop current in the northeastern South China Sea, similar to that induced by a cyclonic eddy. The swift poleward Kuroshio current drives this anticyclonic eddy to become elliptical along the east coast of Taiwan. Whereas for an anticyclonic eddy impinging on the Kuroshio at more northern latitudes, the Ryukyu Islands serve as a waveguide dictating that the eddy propagates toward the east coast of Taiwan (Cheng et al., 2017; Ramp et al., 2017) and, on the other hand, as a barrier restricting the northward movement of the eddy, and therefore the circular eddy is squeezed meridionally to become an elliptic shape with its major axis in the zonal direction. Under this circumstance of the

impinging latitude and eddy size, the Kuroshio in the Luzon Strait is less affected by the westward currents in the southern half of the eddy.

Appendix A: Model Configuration and Validation

The model has 32 layers in the vertical σ-coordinate. The center of each layer in the is designated at −0.001, −0.003, −0.006, −0.008, −0.011, −0.016, −0.020, −0.025, −0.030, −0.034, −0.039, −0.043, −0.048, −0.052, −0.057, −0.061, −0.066, −0.070, −0.075, −0.080, −0.084, −0.089, −0.097, −0.108, −0.125, −0.148, −0.182, −0.261, −0.375, −0.489, −0.659, and −0.886 from the top to the bottom layers. The model topography was constructed using the 2-minute Gridded Global Relief Data (ETOPO2v2, available at http://www.ngdc.noaa.gov/mgg/global/etopo2.html) blended with 1,000 m grid-resolution bathymetric data provided by the Ocean Data Bank of the Ministry of Science and Technology, Taiwan, in the region west of 150°E. The model topography was flat at 6,000 m for depths greater than 6,000 m. This leveling of model topography does not affect the simulated currents in the upper 2,000 m.

The model was initially at rest with an idealized temperature profile given by $T(z) = 2 + 25\exp(z/1{,}000)$. The salinity was constant (34.5) throughout the simulation. The model was spun-up by applying a zonally homogeneous, meridionally varied wind stress, calculated by $\tau_w(y) = -\tau_{w0}\cos(\pi(y-5)/35)$ (where y is latitude and $\tau_{w0} = 0.15$ N m^{-2} is the maximum amplitude of wind stresses) at the sea surface to drive the ocean circulation. The magnitude and meridional variation of the wind stress are consistent with that of the zonally averaged zonal wind stress shown in Figure 3 in Marshall et al. (2007) and Figure 1b in Hu et al. (2015). Furthermore, based on the estimate of Marshall et al. (2007), an idealized, meridionally varied net heat flux, determined using $Q_H(y) = Q_{H0}\cos(\pi(y-5)/35)$ (where $Q_{H0} = 50$ W m^{-2} is the maximum magnitude of heat flux) was applied at the sea surface as the boundary condition. The model was spun-up for 5 years, and the domain-averaged kinetic energy reached a quasi steady state after about 3 years of integration.

Figure Figure A1 shows modeled currents and temperatures at 50 m depth and sea surface height in the western North Pacific after 5 years of integration. The characteristics of the model-simulated circulation in the western North Pacific (Figure Figure A1a), such as the bifurcation of the North Equatorial Current at ∼12°N (Qiu and Chen, 2010) and the Kuroshio's pathway from the east of the Philippines to the south of Japan, agree with the mean velocity and hydrographic features obtained from drifter observations (Centurioni et al., 2004), ship-based measurements (e.g., Liang et al., 2003; Rudnick et al., 2011), and other modeling

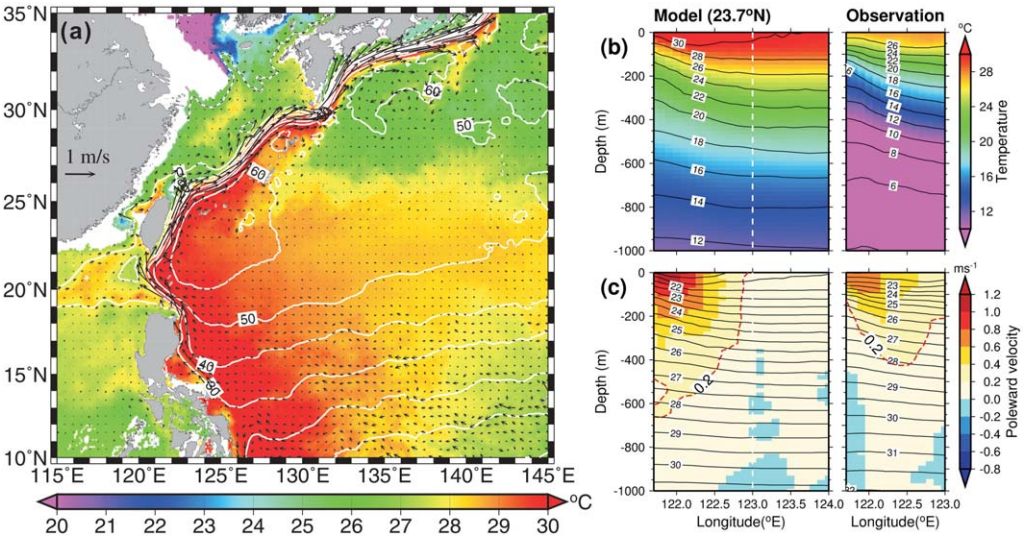

Figure A1. (a) Model-simulated currents (vectors), temperatures (color shaded) at 50 m depth, and sea surface height (contours in cm) in the western North Pacific. Comparisons of modeled and mean observed (b) isotherms and (c) poleward velocity (color shaded) and isopycnals (contours in σt) at a zonal section across the Kuroshio, which is 23.7°N for the model and ∼23.75°N for the observations.

works (Shen et al., 2014, among others). Modeled temperature, meridional velocity (v), and density (σ_t) in a zonal section at 23.7°N are compared with the mean temperature, v, and σ_t calculated from the ship surveys of the 15 cruises at the KTV1 line shown in Figures Figure A1b and Figure A1c. Despite the deviation of the modeled temperature profile from the observations, due to the use of the semi-idealized settings in the model, the isotherm/isopycnal slope across the Kuroshio captures the essential features of the observed mean temperature profile (Figure Figure A1b). The modeled Kuroshio transport of 26.5 Sv (1 Sv = 10^6 m^3 s^{-1}) through the 23.7°N section, integrated from 800 m to the surface and from 121.7°E to 123°E over the region where $v \geq 0.2$ m s^{-1}, is reasonable compared with the observed Kuroshio transport of 21.5 ± 10 Sv at the WOCE PCM-1 section (Johns et al., 2001).

Appendix B: The Setting of the Rankine Vortex Winds

The Rankine Vortex winds, similar to those used in Tsai et al. (2008, 2013), are described by $\frac{V_w^2}{r} + fV_w = \rho_0^{-1} \frac{\partial p}{\partial r}$ (Holland, 1980), where V_w is the orbital wind speed, r is the distance to the vortex wind center, f is the Coriolis parameter, ρ_0 is air density, and p is pressure. The pressure field of the vortex wind was calculated using $p(r) = P_c + (P_n - P_c)\exp(-R_{max}/r)$ (Schloemer, 1954), where P_c is the center pressure of the vortex wind field, R_{max} is the radius of maximum wind, and P_n is the environmental pressure. The size and strength of the eddy were controlled by the duration, central pressure drop, and radius of maximum wind in the Rankine Vortex winds. To quantify model-produced eddies, the Rankine Vortex winds were applied to a model run with no ambient flows, but only an idealized temperature stratification as described previously in this section. A 3 day cyclonic wind field produced by, e.g., $R_{max} = 100$ km and $P_c = 960$ hPa generates a cyclonic eddy with a radial distance from the eddy center to maximum orbital velocity ~100 km (Figure Figure B1a), maximum relative vorticity (ζ) ~0.3f (Figure Figure B1b), and maximum orbital velocity ~0.5 m s^{-1} at 50 m depth in the model (Figure Figure B1a). The inset in Figure Figure B1a shows the vertical structure of temperature and northward velocity in a zonal transect across the cyclonic eddy (black dashed line in Figure Figure B1a) on day 10. The temperature drop in the eddy center is 1.5–2°C in the upper 300 m, and the velocity decreases from 0.5 m s^{-1} near the surface to 0.1 m s^{-1} at approximately 800 m. The isotherm vertical displacement ranges from 100 to 150 m in the upper 300 m to ~50 m at 800 m. The modeled eddy is asymmetric in both its horizontal and vertical hydrographic structures. The orbital velocity and radial gradient of SSH is stronger in the eastern than in the

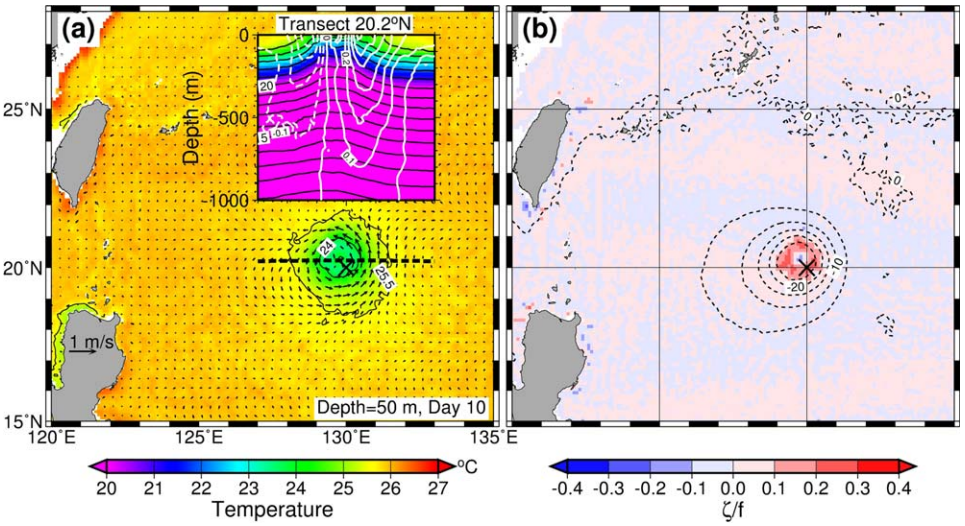

Figure B1. Hydrography and velocity of a cyclonic eddy generated by the Rankine Vortex wind stresses with a center pressure drop of 48 hPa, and a radius of maximum wind of 100 km. The wind stresses were applied at the sea surface for 3 days. (a) Temperature (color shaded) and velocity (arrows) at 50 m depth on day 10. The inset shows temperature (color shaded) and meridional velocity (solid and dashed white lines) in a zonal transect across the cyclonic eddy at 20.2°N. (b) Sea surface height (dashed contours in cm) and the ratio of relative vorticity to the planetary vorticity (ζ/f, color shaded). The relative vorticity was calculated using the velocity at 50 m depth. The symbol "×" marks the initial position of the eddy center.

western half of the eddy. The cyclonic (anticyclonic) eddy drifts northwestward (southwestward) at a speed of 0.1–0.15 m s^{-1} before encountering the Kuroshio.

Acknowledgments
Study of the Kuroshio-II (SK-II) was sponsored by the Ministry of Science and Technology (MOST) grant MOST-101-2611-M-002-018-MY3, MOST 103-2611-M-002-011, and MOST 105-2119-M-002-042. MA was supported by Office of Naval Research (ONR) grants N00014-15-12593 and N00014-16-13069. MHC was sponsored by MOST-101-2611-M-019-002. The captains and crew members of the R/Vs Ocean Researcher I and V, and technicians W.-H. Ho, W.-H. Lee (deceased), H.-C. Hsieh, and B. Wang assisted the ship surveys. AVISO SSH and associated products are available at http://www.aviso.oceanobs.com/en/data/products.html. The bathymetric data ETOPO2v2 can be downloaded at http://www.ngdc.noaa.gov/mgg/global/etopo2.html. The Ocean Data Bank of Taiwan archives processed ship survey and PIES data that are used in this study at http://ctd.oc.ntu.edu.tw/doi_data/obs/ and the model-data and associated source code of the model at http://ctd.oc.ntu.edu.tw/doi_data/model/.

References

Andres, M., & Cenedese, C. (2013). Laboratory experiments and observations of cyclonic and anticyclonic eddies impinging on an island. *Journal of Geophysical Research: Oceans*, *118*, 762–773. https://doi.org/10.1002/jgrc.20081

Andres, M., Mensah, V., Jan, S., Chang, M.-H., Yang, Y. J., Lee, C. M., . . . Sanford, T. B. (2017). Downstream evolution of the Kuroshio's time varying transport and velocity structure. *Journal of Geophysical Research: Oceans*, *122*, 3519–3542. https://doi.org/10.1002/2016JC012519

Blumberg, A. F., & Mellor, G. F. (1987). A description of a three dimensional coastal ocean circulation model. In N. Heaps (Ed.), *Three-dimensional coastal ocean models, coastal and estuarine stud* (Vol. 4, pp. 1–16). Washington DC: American Geophysical Union.

Centurioni, L. R., Niller, P. P., & Lee, D. K. (2004). Observations of inflow of Philippine Sea surface water into the South China Sea through the Luzon Strait. *Journal of Physical Oceanography*, *34*, 113–121. https://doi.org/10.1175/1520-0485(2004)034<0113:OOIOPS>2.0.CO;2

Chang, Y., Miyazawa, Y., & Guo, X. (2015). Effects of the STCC eddies on the Kuroshio based on the 20-year JCOPE2 reanalysis results. *Progress in Oceanography*, *135*, 64–76. https://doi.org/10.1016/j.pocean.2015.04.006

Chang, Y., & Oey, L. (2012). The Philippines-Taiwan 746 oscillation: Monsoon like interannual oscillation of the subtropical-tropical western North Pacific wind system and its impact on the ocean. *Journal of Climate*, *25*(5), 1597–1618. https://doi.org/10.1175/JCLI-D-11-00158.1

Cheng, Y.-H., Ho, C.-R., Zheng, Q., Bo, Q., Hu, J., & Kuo, N.-J. (2017). Statistical features of eddies approaching the Kuroshio east of Taiwan Island and Luzon Island. *Journal of Oceanography*, *73*(6), 427–483. https://doi.org/10.1007/s10872-017-0411-7

Cheng, Y.-H., Ho, C.-R., Zheng, Q., & Kuo, N.-J. (2014). Statistical characteristics of mesoscale eddies in the North Pacific derived from satellite altimetry. *Remote Sensing*, *6*(6), 5164–5183. https://doi.org/10.3390/rs6065164

Chern, C.-S., & Wang, J. (2005). Interactions of mesoscale eddy and western boundary current: A reduced-gravity numerical model study. *Journal of Oceanography*, *61*(2), 271–282.

Clément, L., Frajka-Williams, E., Sheen, K. L., Brearley, J. A., & Naveira Garabato, A. C. (2017). Generation of internal waves by eddies impinging on the western boundary of the North Atlantic. *Journal of Physical Oceanography*, *46*, 1067–1079. https://doi.org/10.1175/JPO-D-14-0241.1

Fofonoff, N. P., & Millard, R. C. Jr. (1983). *Algorithms for computation of fundamental properties of seawater* (UNESCO Tech. Pap. in Mar. Sci. 44, 53 pp.). Paris, France: Division of Marine Sciences, UNESCO.

Gill, A. E., Green, J. S. A., & Simmons, A. J. (1974). Energy partition in the large-scale ocean circulation and the production of mid-ocean eddies. *Deep Sea Research and Oceanography Abstracts*, *21*, 499–528. https://doi.org/10.1016/0011-7471(74)90010-2

Holland, G. J. (1980). An analytic model of the wind and pressure profiles in hurricanes. *Monthly Weather Review*, *108*, 1212–1218. https://doi.org/10.1175/1520-0493(1980)108<1212:AAMOTW>2.0.CO;2

Hsin, Y.-C., Qiu, B., Chiang, T.-L., & Wu, C.-R. (2013). Seasonal to interannual variations in the intensity and central position of the surface Kuroshio east of Taiwan. *Journal of Geophysical Research*, *118*, 4305–4316. https://doi.org/10.1002/jgrc.20323

Hu, D. X., Wu, L. X., Cai, W. J., Sen Gupta, A., Ganachaud, A., Qiu, B., . . . Kessler, W. S. (2015). Pacific western boundary currents and their roles in climate. *Nature*, *522*, 299–308. https://doi.org/10.1038/nature14504

Hwang, C., Wu, C.-R., & Kao, R. (2004). TOPEX/Poseidon observations of mesoscale eddies over the subtropical countercurrent: Kinematic characteristics of an anticyclonic eddy and a cyclonic eddy. *Journal of Geophysical Research*, *109*, C08013. https://doi.org/10.1029/2003JC002026

Jan, S., Yang, Y. J., Wang, J., Mensah, V., Kuo, T.-H., Chiou, M.-D., . . . Chien, H. (2015). Large variability of the Kuroshio at 23.75°N east of Taiwan. *Journal of Geophysical Research: Oceans*, *120*, 1825–1840. https://doi.org/10.1002/2014JC010614

Johns, W. E., Lee, T. N., Zhang, D., Zantopp, R., Liu, C.-T., & Yang, Y. (2001). The Kuroshio east of Taiwan: Moored transport observations from the WOCE PCM-1 array. *Journal of Physical Oceanography*, *31*, 1031–1053. https://doi.org/10.1175/1520-0485(2001)031<1031:TKEOTM>2.0.CO;2

Kuo, Y.-C., & Chern, C.-S. (2011). Numerical study on the interactions between a mesoscale eddy and a western boundary current. *Journal of Oceanography*, *67*, 263–272. https://doi.org/10.1007/s10872-011-0026-3

Kuo, Y.-C., Chern, C.-S., & Zheng, Z.-W. (2017). Numerical study on the interactions between the Kuroshio current in the Luzon Strait and a mesoscale eddy. *Ocean Dynamics*, *67*(3–4), 369–381. https://doi.org/10.1007/s10236-017-1038-3

Lee, I.-H., Ko, D., Wang, Y.-H., Centurioni, L., & Wang, D.-P. (2013). The mesoscale eddies and Kuroshio transport in the western North Pacific east of Taiwan from 8-year (2003–2010) model reanalysis. *Ocean Dynamics*, *63*(9), 1027–1040. https://doi.org/10.1007/s10236-013-0643-z

Liang, W.-D., Tang, T. Y., Yang, Y. J., Ko, M. T., & Chuang, W.-S. (2003). Upper-ocean currents around Taiwan. *Deep Sea Research Part II*, *50*, 1085–1105. https://doi.org/10.1016/S0967-0645(03)00011-0

Lien, R.-C., Ma, B., Cheng, Y.-H., Ho, C.-R., Qiu, B., Lee, C. M., & Chang, M.-H. (2014). Modulation of Kuroshio transport by mesoscale eddies at the Luzon Strait entrance. *Journal of Geophysical Research: Oceans*, *119*, 2129–2142. https:/doi.org//10.1002/2013JC009548

Liu, W., Liu, Q., & Jia, Y. (2004). The Kuroshio transport east of Taiwan and the sea surface height anomaly from the interior ocean. *Journal of Ocean University of China*, *3*(2), 135–140. https://doi.org/10.1007/s11802-004-0023-x

Liu, Y., Dong, C., Guan, Y., Chen, D., McWilliams, J., & Nencioli, F. (2012). Eddy analysis in the subtropical zonal band of the North Pacific Ocean. *Deep Sea Research Part I*, *68*, 54–67. https://doi.org/10.1016/j.dsr.2012.06.001

Marshall, J., Ferreira, D., Campin, J.-M., & Enderton, D. (2007). Mean climate and variability of the atmosphere and ocean on an aquaplanet. *Journal of the Atmospheric Sciences*, *64*, 4270–4286. https://doi.org/10.1175/2007JAS2226.1

Meinen, C. S., & Watts, D. R. (2000). Vertical structure and transport on a transect across the North Atlantic Current near 428N: Time series and mean. *Journal of Geophysical Research*, *105*, 21869–21891. https://doi.org/10.1029/2000JC900097

Mensah, V., Andres, M., Lien, R.-C., Ma, B., Lee, C., & Jan, S. (2016). Combining observations from multiple platforms across the Kuroshio northeast of Luzon: a highlight on PIES data. *Journal of Atmospheric and Oceanic Technology*, *33*, 2185–2203. https://doi.org/10.1175/JTECH-D-16-0095.1

Qiu, B. (1999). Seasonal eddy field modulation of the North Pacific Subtropical Cuntercurrent: TOPEX/Poseidon observations and theory. *Journal of Physical Oceanography*, *29*, 2471–2486.

Qiu, B., & Chen, S. (2010). Interannual-to-decadal variability in the bifurcation of the North Equatorial Current off the Philippines. *Journal of Physical Oceanography*, *40*, 2525–2538. https://doi.org/10.1175/2010JPO4462.1

Ramp, S., Colosi, J. A., Worcester, P. F., Bahr, F. L., Heaney, K. D., Mercer, J. A., & Van Uffelen, L. J. (2017). Eddy properties in the subtropical countercurrent, Western Philippine Sea. *Deep Sea Research Part I*, *125*, 11–25. https://doi.org/10.1016/j.dsr.2017.03.010

Roemmich, D., & Gilson, J. (2001). Eddy transport of heat and thermocline waters in the North Pacific: A Key to interannual/decadal climate variability? *Journal of Physical Oceanography*, *31*, 675–687. https://doi.org/10.1175/1520-0485(2001)031<0675:ETOHAT>2.0.CO;2

Rudnick, L. D., Jan, S., Centurioni, L., Lee, C., Lien, R.-C., Wang, J., . . .Chern, C.-S. (2011). Seasonal and mesoscale variability of the Kuroshio near its origin. *Oceanography*, *24*(4), 52–63. https://doi.org/10.5670/oceanog.2011.94

Schloemer, R. W. (1954). *Analysis and synthesis of hurricane wind patterns over Lake Okechobee, Florida* (Hydromet. Rep. 31). Washington, DC: Department of Commerce.

Shen, M.-L., Tseng, Y.-H., Jan, S., Young, C.-C., & Chiou, M.-D. (2014). Long-term variability of the Kuroshio transport east of Taiwan and the climate it conveys. *Progress in Oceanography*, *121*, 60–73. https://doi.org/10.1016/j.pocean.2013.10.009

Sheu, W.-J., Wu, C.-R., & Oey, L.-Y. (2010). Blocking and westward passage of eddies in the Luzon Strait. *Deep Sea Research Part II*, *57*, 1783–1791. https://doi.org/10.1016/j.dsr2.2010.04.004

Sun, C., & Watts, D. R. (2001). A circumpolar gravest empirical mode for the Southern Ocean hydrography. *Journal of Geophysical Research*, *106*, 2833–2855. https://doi.org/10.1029/2000JC900112

Tsai, C.-J., Andres, M., Jan, S., Mensah, V., Sanford, T. B., Lien, R.-C., & Lee, C. M. (2015). Eddy-Kuroshio interaction processes revealed by mooring observations off Taiwan and Luzon. *Geophysical Research Letters*, *42*, 8098–8105. https://doi.org/10.1002/2015GL065814

Tsai, Y. L., Chern, C.-S., Jan, S., & Wang, J. (2013). Numerical study of Cold Dome variability induced by Typhoon Morakot (2009) off Northeastern Taiwan. *Journal of Marine Research*, *71*(1–2), 109–132.

Tsai, Y. L., Chern, C.-S., & Wang, J. (2008). Typhoon induced upper ocean cooling off northeastern Taiwan. *Geophysical Research Letters*, *35*(14), L14605. https://doi.org/10.1029/2008GL034368

Vélez-Belchí, P., Centurioni, L. R., Lee, D.-K., Jan, S., & Niiler, P. P. (2013). Eddy induced Kuroshio intrusions onto the continental shelf of the East China Sea. *Journal of Marine Research*, *71*(1–2), 83–108.

Waseda, T., Mitsudera, H., Taguchi, B., & Yoshikawa, Y. (2002). On the eddy-Kuroshio interaction: Evolution of the mesoscale eddy. *Journal of Geophysical Research*, *107*(C8), 3088. https://doi.org/10.1029/2000JC000756

Watts, D. R., Sun, C., & Rintoul, S. (2001). Two-dimensional gravest empirical modes determined from hydrographic observations in the Subantarctic Front. *Journal of Physical Oceanography*, *31*, 2186–2209. https://doi.org/10.1175/1520-0485(2001)031<2186:ATDGEM>2.0.CO;2

Wunsch, C. (1998). The work done by the wind on the oceanic general circulation. *Journal of Physical Oceanography*, *28*, 2332–2340. https://doi.org/10.1175/1520-0485(1998)028<2332:TWDBTW>2.0.CO:2

Yan, X., Zhu, X.-H., Pang, C., & Zhang, L. (2016). Effects of mesoscale eddies on the volume transport and branch pattern of the Kuroshio east of Taiwan. *Journal of Geophysical Research: Oceans*, *121*, 7683–7700. https://doi.org/10.1002/2016JC012038

Yang, G., Wang, F., Li, Y., & Lin, P. (2013). Mesoscale eddies in the northwestern subtropical Pacific Ocean: Statistical characteristics and three-dimensional structures. *Journal of Geophysical Research: Oceans*, *118*, 1906–1925. https://doi.org/10.1002/jgrc.20164

Yang, K.-C., Wang, J., Lee, C. M., Ma, B., Lien, R.-C., Jan, S., . . . Chang, M.-H. (2015). Two mechanisms cause dual velocity maxima in the Kuroshio east of Taiwan. *Oceanography*, *28*(4), 64–73. https://doi.org/10.5670/oceanog.2015.82

Yang, Y., Liu, C.-T., Hu, J.-H., & Koga, M. (1999). Taiwan current (Kuroshio) and impinging eddies. *Journal of Oceanography*, *55*, 609–617. https://doi.org/10.1023/A:1007892819134

Yuan, Y., Kaneko, A., Su, J., Zhu, X., Liu, Y., Gohda, N., & Chen, H. (1998). The Kuroshio east of Taiwan and in the East China Sea and the currents east of Ryukyu Islands during early summer of 1996. *Journal of Oceanography*, *54*, 217–226.

Zhang, D., Lee, T., Johns, W., Liu, C., & Zantopp, R. (2001). The Kuroshio east of Taiwan: Modes of variability and relationship to interior mesoscale eddies. *Journal of Physical Oceanography*, *31*(4), 1054–1074. https://doi.org/10.1175/1520-0485(2001)031<1054:TKEOTM>2.0.CO;2